Journal of Catalysis 280 (2011) 206–220

Contents lists available at ScienceDirect

Journal of Catalysis

journal homepage: www.elsevier.com/locate/jcat

Influence of particle size on the activity and stability in steam methane reforming of supported Rh nanoparticles

D.A.J.M. Ligthart, R.A. van Santen, E.J.M. Hensen *

Schuit Institute of Catalysis, Eindhoven University of Technology, P.O. Box 513, 5600 MB Eindhoven, The Netherlands

ARTICLE INFO

Article history:
Received 13 January 2011
Revised 10 March 2011
Accepted 20 March 2011
Available online 6 May 2011

Keywords:
Steam methane reforming
Rhodium
Particle size
Reaction mechanism
Deactivation

ABSTRACT

The influence of Rh nanoparticle size and type of support on the catalytic performance in steam methane reforming has been investigated to clarify the nature of the rate-controlling step. A set of Rh catalysts was prepared using ZrO_2, CeO_2, $CeZrO_2$ and SiO_2 supports. The nature and dispersion of the active Rh metal phase was studied by H_2-chemisorption, TEM and X-ray absorption spectroscopy. The particle size was varied between 1 and 9 nm. The degree of Rh reduction depends on the particle size and the support. Very small particles cannot be fully reduced, especially when ceria is the support. The intrinsic rate per surface metal atom increases linearly with the Rh metal dispersion and does not depend on the type of support. With the support of kinetic data, it is concluded that dissociative CH_4 adsorption is the single rate-controlling step at least at reaction temperatures above 325 °C. This implies that the overall rate is controlled by the density of low-coordinated edge and corner metal atoms in the nanoparticles. These particles contain sufficient step edge sites to provide an easy reaction pathway for C—O recombination reactions. Catalysts with Rh nanoparticles smaller than 2.5 nm deactivate more strongly than catalysts with larger nanoparticles. Characterization of spent catalysts by X-ray absorption spectroscopy shows that deactivation is due to the oxidation of very small particles under the steam methane reforming reaction conditions.

© 2011 Elsevier Inc. All rights reserved.

1. Introduction

Steam reforming of natural gas and light hydrocarbons remains the preferred route for the production of syngas (a mixture of CO and H_2) and hydrogen. Syngas is a key intermediate in the chemical industry for production of a wide range of higher value fuels and chemicals such as clean synthetic diesel and gasoline olefins via the Fischer–Tropsch synthesis (FTS), methanol by the methanol process and hydrogen by the water–gas shift (WGS) reaction. Hydrogen is primarily used for the synthesis of ammonia and for hydrotreating purposes in petroleum refineries [1,2]. Steam methane reforming (SMR) was already commercialized in the 1960s, and Ni has remained the preferred transition metal in reforming catalysts ever since [3,4]. Besides Ni, a number of other transition metals exhibit high catalytic activity in SMR, most notably Rh and Ru [5–7], although the exact activity trend among these metals remains debated [7,8]. An issue of considerable debate is the exact nature of the reaction mechanism [9] and especially the identification of the rate-controlling step [1,7,10]. Although Iglesia and co-workers [10] have shown that methane dissociation is rate-controlling, Jones et al. [7] have recently reported that both CH_4 dissociation and C—O recombination reactions determine the overall reaction rate for metals such as Rh and Ru.

The rate-controlling step will critically depend on the exact reaction conditions and also on the particle size. To understand this in detail, the dependence of the rates of the three-candidate rate-controlling elementary reaction steps in the SMR reaction, i.e., (i) dissociative adsorption of methane, (ii) surface recombination of C and O to carbon monoxide and (iii) dissociation of water [11], on the particle size will be briefly discussed. Nanoparticles expose terrace, edge and corner atoms with respective metal–metal coordination numbers of 9 (for the most dense surface of *fcc* and *hcp* metals), 7 and 6 at their surfaces (Fig. 1). Dissociative CH_4 adsorption involves the cleavage of a σ bond, which typically occurs over a single surface metal atom [12,13]. The energy barrier for this elementary reaction step will decrease with increasing coordinative unsaturation of the metal surface atoms because of the stronger binding of the CH_3 and H intermediates in the transition state. Thus, one expects that the rate of methane dissociation will increase with increasing dispersion, because smaller particles expose a larger fraction of edge and corner atoms at their surface.

The particle size dependence for C—O bond formation reactions is very different. C–O recombination proceeds with a relatively high energy barrier on terrace surfaces [14–16]. It has been established that the dissociation and association reactions of diatomic

* Corresponding author.
E-mail address: e.j.m.hensen@tue.nl (E.J.M. Hensen).

0021-9517/$ - see front matter © 2011 Elsevier Inc. All rights reserved.
doi:10.1016/j.jcat.2011.03.015

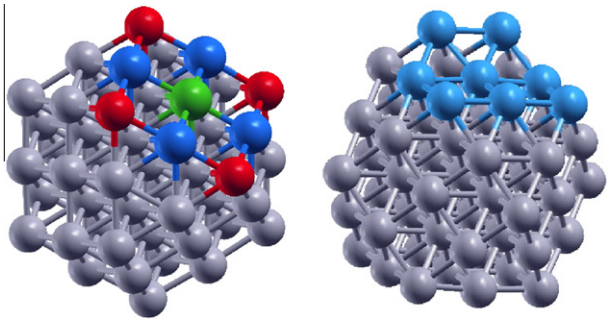

Fig. 1. An octahedral Rh nanoparticle of 1 nm (55 Rh atoms): (left) terrace, edge and corner atoms are shown in green, blue and red, respectively; (right) with created B_5-sites.

molecules with π-bonds such as CO, N_2 and NO are preferred over sites with a particular geometry involving an ensemble of five or six metal atoms arranged in such fashion that a step site is created (Fig. 1). The reason is that the specific surface topology of such steps avoids metal atoms sharing between the dissociating fragments (the C and O atoms in the case of CO formation). An additional factor is the involvement of a larger number of surface metal atoms in the bonding of the transition state complex as compared to the terrace surface. Van Hardeveld and Hartog [17] have predicted that the density of these step edge sites is maximal for metal nanoparticles in the range 1.8–2.5 nm. These authors introduced the term "B_5 sites" [18], which are very similar to the "F_6 sites" considered by the group of Van Santen [19,20]. Besides recombination of surface C and O adatoms, an alternative pathway involving the oxymethylidyne (HCO, formyl) intermediate [21,22]. For each of the Rh(1 1 1) and Rh(2 1 1) surfaces, Van Grootel et al. [23] found that the activation barriers for the C + O and CH + O pathways are very similar. The barrier on the stepped surface is about half that on the terrace. An alternative CH route involving a COH intermediate [24] is much less favourable [19,23,25]. The important corollary of these considerations is that an optimal particle size of about 2 nm can be expected for steam methane reforming, if C–O bond formation is rate-controlling.

The dissociation of water into OH and H fragments was shown to be independent of the Rh surface atom coordinative unsaturation [26]. An alternative pathway involves the reaction of water with atomic oxygen to produce two hydroxyl groups. Although the energy barrier for this reaction is lower than that for unpromoted water dissociation, the cost for oxygen diffusion to the site next to adsorbed water results in a very similar overall activation barrier [26]. Based on the limited number of works on water activation, it can be assumed that water dissociation is independent of the particle size under conditions where the formation of hydrogen-bonded networks of OH/H_2O adsorbates is absent [27].

Jones et al. [7] have shown that the intrinsic reaction rate of steam methane reforming at 500 °C over supported Rh particles increases in a nearly linear manner for a set of catalysts with particle sizes larger than 3 nm. This temperature is typical for the inlets of industrial reformers and refers to the situation in which the effectiveness factor of the catalyst is high. Based on the range of Rh particle sizes considered by Jones et al. [7], it is not possible to unequivocally conclude on the nature of the rate-controlling step, and both CH_4 dissociation and C—O recombination reactions remain candidate. It may also be that with a decrease in the particle size, the rate-controlling step changes from CH_4 dissociation to C—O recombination. Wei and Iglesia [10] have used a wider range of Rh particle size supported on alumina and zirconia and argued that methane dissociation is always the rate-controlling step. The reaction temperature in this case was 600 °C. It can be argued that methane dissociation will be rate-controlling at high temperature because of entropy considerations [23]. Van Grootel et al. [23] have also shown for rhodium that H_2O dissociation will always be faster than dissociative CH_4 adsorption and C—O recombination.

To unequivocally conclude on the issue of the rate-controlling step in SMR at relatively low temperatures, a set of supported Rh catalysts have been prepared with a wide range of particle sizes (1–9 nm) and with a wider range of support materials than employed before. Characterization focused on the nature and dispersion of the active Rh metal phase (dispersion, reduction degree). Intrinsic reaction kinetics was determined with the aim of determining the nature of the rate-controlling step as a function of the particle size. An additional issue that became apparent in the course of our investigations is the deactivation of Rh catalysts that contain metal nanoparticles smaller than ~2.5 nm. Part of our efforts therefore focused on elucidating the reason for this deactivation of very small nanoparticles.

2. Experimental methods

2.1. Support materials

Zirconia (Gimex RC-100 with 99.74% ZrO_2 and 0.13% TiO_2) was kindly provided by Gimex. A high-porosity cerium-doped zirconium hydroxide with a nominal composition of $Ce_{0.25}Zr_{0.75}O_2$ was supplied by MEL Chemicals. Silica was kindly provided by Shell. Ceria was prepared by homogeneous precipitation of Ce^{3+} following urea decomposition [28,29]. In a typical synthesis, 95 g of urea (Merck, purity 99%) and 100 g of $Ce(NO_3)_3{\cdot}6H_2O$ (Acros, purity 99.5%) were dissolved in 1.2 L deionized water. The solution was heated under stirring in a double-walled vessel at 95 °C for 14 h. The pH was recorded during synthesis. Subsequently, the precipitate was filtered, washed with deionized water at 70 °C, dried in an oven overnight and calcined.

Nanostructured ceria supports were obtained by dissolving 8.68 g $Ce(NO_3)_3{\cdot}6H_2O$ in 15 ml of deionized water. The solution was mixed and stirred with 10 ml 6 M NaOH solution before another 30 ml of 7.7 M NaOH solution was added. The milky slurry formed was transferred into a Teflon-lined stainless steel autoclave. Before the autoclave was closed, 35 ml of deionized water was added under vigorous stirring. The mixture was kept in an oven for 24 h at 100 °C or 180 °C to obtain ceria nanorods or nanocubes, respectively [30]. The precipitate was filtrated, washed and dried in an oven overnight. The ceria nanorods and nanocubes were yellow and white, respectively. These materials were calcined at 500 °C.

The oxide supports will be denoted by $S(T)$, with S the support material and T the calcination temperature (°C). The nanostructured ceria catalysts are named CeO_2-rod and CeO_2-cube.

2.2. Catalyst preparation

A series of supported Rh catalysts were prepared by pore volume impregnation using aqueous solutions of $Rh(NO_3)_3{\cdot}nH_2O$ (Riedel de Haën, purity 99.9%) of appropriate concentration. Each support material was sieved into a fraction of 125–250 μm. Prior to impregnation, the support was calcined in a mixture of 20 vol.% O_2 in N_2 at a flow rate of 100 ml/min, while being heated at a rate of 2 °C/min (5 °C/min for CeO_2 supports) to the final temperature followed by an isothermal period of 4 h. The impregnated supports were dried for 3 h in air and at 110 °C overnight before further treatment.

Different Rh particle sizes were obtained by varying the support, the Rh loading, the calcination temperature of the support, the calcination temperature of the impregnated catalyst and an

ageing procedure. The metal loading was varied between 0.1 and 1.6 wt.% Rh. The catalyst precursors were calcined at 600 °C (550 °C for Rh supported on CeO_2) and 900 °C and aged at 750, 900, and 1000 °C in a 1:1 H_2O/H_2 mixture at ambient pressure for 62.5 h.

Hereafter, the catalysts will be denoted by Rh(x, aT) with x the metal loading (wt.%), a optionally indicating an ageing treatment and T the final catalyst treatment temperature (°C) followed by the support reference. The complete set of catalysts and their most important properties are listed in Tables 1 and 2.

2.3. Catalyst characterization

2.3.1. Elemental analysis

The metal loading was determined by inductively coupled plasma atomic emission spectroscopy (ICP-AES) analyses performed on a Goffin Meyvis SpectroCirus^{ccd} apparatus. For CeO_2-supported catalysts, an amount of sample was dissolved in a 1:1 H_2O/H_2SO_4 solution. A solution of 5 M $(NH_4)_2SO_4$ in H_2SO_4 was employed to extract rhodium from the ZrO_2-containing catalysts. Typically, an amount of sample was stirred in the acid under heating until a clear solution was obtained. The SiO_2-supported catalysts were dissolved in a 1:1:1 $HF/HNO_3/H_2O$ solution under mild heating.

2.3.2. Nitrogen physisorption

Surface areas were measured with a Micromeritics TriStar 3000 BET apparatus by nitrogen physisorption at −195 °C after outgassing the sample for 3 h under vacuum at 150 °C.

2.3.3. X-ray diffraction (XRD)

XRD analysis was carried out on a Bruker D4 Endeavor Diffractometer using Cu Kα-radiation (λ = 1.54056 Å). With a step size of 0.099° and a time per step of 1 s, 2θ angles from 20° to 80° were measured. The crystal structure of the support materials was determined by using the PDF database.

2.3.4. Hydrogen chemisorption

H_2-chemisorption was carried out at −80 °C using a Micromeritics ASAP 2020C setup equipped with an isopropanol bath cooled by a thermostat (Thermo EK 90). Before analysis, an amount of sample was oxidized at 500 °C. After an isothermal period of 1 h, the sample was reduced at 450 °C for 2 h and evacuated for 4.5 h. The double isotherm method with an intermediate vacuum treatment of 1 h was employed to determine the irreversibly bound chemisorbed hydrogen. To calculate the metal dispersion, an adsorption stoichiometry of one hydrogen atom per surface rhodium atom was assumed [31].

2.3.5. Transmission electron microscopy (TEM)

Transmission electron micrographs were acquired on a FEI Tecnai 20 transmission electron microscope at an acceleration voltage of 200 kV with a LaB6 filament. Typically, a small amount of grinded sample was reduced at 500 °C and passivated in 1 vol.% O_2 in He for 2 h before being suspended in pure ethanol, sonicated and dispersed over a Cu grid with a holey carbon film. TEM images were recorded using a $1k \times 1k$ Gatan CCD camera at different magnifications. From the electron micrographs, the metal nanoparticle diameters were determined from the projected area of the particles assuming that the particles are spherical. The particle size distribution was determined from analysis of around 100 up to 300 particles from at least three different micrographs.

2.3.6. X-ray absorption spectroscopy

X-ray absorption measurements were carried out at the Dutch-Belgian Beamline (Dubble) at the European Synchrotron Radiation Facility (ESRF), Grenoble, France (storage ring 6.0 GeV, ring current 200 mA). Data were collected at the Rh K-edge in fluorescence mode with a nine-channel solid-state detector. Energy selection was done by a double crystal Si (1 1 1) monochromator. Background removal was carried out by standard procedures. EXAFS analysis was then performed with EXCURVE931 on k^3-weighted unfiltered raw data using the curved wave theory. Phase shifts were derived from ab initio calculations using Hedin-Lundqvist exchange potentials and Von Barth ground states. Energy calibration was carried out with Rh foil. The amplitude reduction factor S_0^2 associated with central atom shake-up and shake-off effects was set at 1.0 by calibration of the first- and second shell Rh–Rh coordination numbers to 12 and 6, respectively, for the k^3-weighted EXAFS fits of the Rh foil. The structure of the Rh metal foil and the first two shells of the FT EXAFS spectrum of Rh_2O_3 correspond

Table 1
Textural properties of the various support precursors before and after calcination.

Support	Precursor	S.A.[a] (m^2/g)	P.V.[b] (ml/g)	$T_{calcination}$ (°C)	S.A. (m^2/g)	P.V. (ml/g)	Phase[c] XRD	d_{XRD}[d] (nm)
ZrO_2	ZrO_2 RC-100 (Gimex)	101	0.31	350	92	0.46	*t, m*	n.d.
				450	79	0.45	*m*	12
				600	57	0.41	*m*	14
				750	34	0.32	*m*	20
				900	9	0.16	*m*	31
CeO_2	$Ce(CO_3)OH$	n.d.	n.d.	350	106	0.12	*f*	n.d.
				450	93	0.09	*f*	16
				550	60	0.09	*f*	21
				650	16	0.09	*f*	31
				900	1	0.09	*f*	48
CeO_2-rod	CeO_2-rod	98	0.18	500	81	0.18	*f*	n.d.
CeO_2-cube	CeO_2-cube	15	0.09	500	15	0.09	*f*	n.d.
$CeZrO_2$	$Ce_{0.25}Zr_{0.75}O_2$ (MEL)	271	0.46	350	154	0.36	*t*	n.d.
				450	109	0.29	*t*	6
				600	84	0.29	*t*	7
				750	53	0.29	*t*	9
				900	17	0.20	*t*	19
SiO_2	SiO_2 (Shell)	209	1.25	–	205	1.25	–	–
				900	151	1.10	–	–

[a] Surface area.
[b] Pore volume by water.
[c] Phase identified by XRD (t = tetragonal; m = monoclinic; f = fluorite).
[d] Particle size computed by Scherrer equation from line broadening of XRD reflections.

Table 2
Textural properties, metal loading and notation of the catalysts.

Rh/Support	$T_{calcination}$ (°C)	Rh loading[a] (wt.%)	S.A. (m^2/g)	Catalyst label
ZrO_2(600)	600	0.11	–	Rh(0.1, 600)/ZrO_2(600)
		0.45	57	Rh(0.4, 600)/ZrO_2(600)
		0.82	-	Rh(0.8, 600)/ZrO_2(600)
		1.62	57	Rh(1.6, 600)/ZrO_2(600)
ZrO_2(900)	600	0.39	9	Rh(0.4, 600)/ZrO_2(900)
		1.60	–	Rh(1.6, 600)/ZrO_2(900)
	900	1.60	7	Rh(1.6, 900)/ZrO_2(900)
	Age750[b]	1.62	9	Rh(1.6, a750)/ZrO_2(900)
	Age900[b]	1.65	4	Rh(1.6, a900)/ZrO_2(900)
	Age1000[b]	1.72	2	Rh(1.6, a1000)/ZrO_2(900)
CeO_2(550)	550	0.15	–	Rh(0.1, 550)/CeO_2(550)
		0.46	60	Rh(0.4, 550)/CeO_2(550)
		0.98	60	Rh(0.8, 550)/CeO_2(550)
		1.92	59	Rh(1.6, 550)/CeO_2(550)
CeO_2(900)	550	0.47	1	Rh(0.4, 550)/CeO_2(900)
		1.56	1	Rh(1.6, 550)/CeO_2(900)
	900	1.62	1	Rh(1.6, 900)/CeO_2(900)
	Age750[b]	1.52	-	Rh(1.6, a750)/CeO_2(900)
	Age900[b]	1.60	1	Rh(1.6, a900)/CeO_2(900)
	Age1000[b]	1.52	–	Rh(1.6, a1000)/CeO_2(900)
CeO_2-rod	500	0.14	72	Rh(0.1, 500)/CeO_2-rod(500)
		1.63		Rh(1.6, 500)/CeO_2-rod(500)
CeO_2-cube	500	1.58	15	Rh(1.6, 500)/CeO_2-cube(500)
$CeZrO_2$(600)	600	0.12	84	Rh(0.1, 600)/$CeZrO_2$(600)
		0.46	–	Rh(0.4, 600)/$CeZrO_2$(600)
		0.91	–	Rh(0.8, 600)/$CeZrO_2$(600)
		1.79	84	Rh(1.6, 600)/$CeZrO_2$(600)
$CeZrO_2$(900)	600	0.51	19	Rh(0.4, 600)/$CeZrO_2$(900)
		1.71	–	Rh(1.6, 600)/$CeZrO_2$(900)
	900	1.66	17	Rh(1.6, 900)/$CeZrO_2$(900)
	Age900[b]	1.72	6	Rh(1.6, a900)/$CeZrO_2$(900)
	Age1000 [b]	1.75	3	Rh(1.6, a1000)/$CeZrO_2$(900)
SiO_2	550	0.10	–	Rh(0.1, 550)/SiO_2
		0.33	–	Rh(0.4, 550)/SiO_2
		0.79	213	Rh(0.8, 550)/SiO_2
		1.59	210	Rh(1.6, 550)/SiO_2
SiO_2(900)	550	0.65	–	Rh(0.8, 550)/SiO_2(900)
		1.58	149	Rh(1.6, 550)/SiO_2(900)
	900	1.51	150	Rh(1.6, 900)/SiO_2(900)
	Age750[b]	1.18	108	Rh(1.6, a750)/SiO_2(900)
	Age900[b]	1.01	40	Rh(1.6, a900)/SiO_2(900)

Note: The systems were calcined for 4 h or aged for 62.5 h at various temperatures after impregnation.
[a] Determined by ICP-AES.
[b] Ageing in a mixture of H_2O and H_2.

well to literature data [32,33]. The near-edge region of the absorption spectra of these reference compounds were used to fit the near-edge region of the catalysts.

Spectra at the Rh *K*-edge were recorded in a stainless-steel-controlled atmosphere cell. The cell was heated with two firerods controlled by a temperature controller. A thermocouple was placed close to the catalyst sample. Typically, an amount of 200 mg of sample was pressed in a stainless steel holder and placed in the cell. Carbon foils were held between two high-purity carbon spacers with a thickness of 1000 μm. High-purity gases (He and H_2) were delivered by thermal mass flow controllers. The total gas flow was kept at 50 ml/min. The catalyst sample was heated at a rate of 10 °C/min up to a final temperature of 500 °C, whilst recording XANES spectra. After reduction at this temperature for 1 h, the sample was cooled and two EXAFS spectra were recorded.

2.4. Catalytic activity in steam methane reforming

The catalytic activity in steam methane reforming was measured using a fixed-bed reactor with an internal diameter of 6 mm. The stainless steel reactor tube was placed in a solid brass body to ensure isothermal operation of the reactor. Typically, 3–15 mg of catalyst (sieved to 125–250 μm) was mixed with inert α-Al_2O_3 (purity 99.997%, 110 μm crystalline, surface area 5.5 m^2/g). Prior to catalytic activity measurements, the catalysts were oxidized at 500 °C for 1 h in 3 vol.% O_2 in N_2 and subsequently reduced at 450 °C for 2 h in 20 vol.% H_2 in N_2. The composition of the effluent gas was analysed by online gas chromatography (Interscience GC-8000 Top) with a ShinCarbon ST 80/100 packed column (2 mm × 2 m) and a thermal conductivity detector. SMR was carried out at 500 °C with a feed containing 5 vol.% CH_4 and 15 vol.% H_2O in He (H/C = 10 and O/C = 3) at a total pressure of 1.2 bar. The total gas flow was 200 ml/min. All tubings were kept at 125 °C after the point of steam introduction to avoid condensation. The conversion was calculated from the effluent concentrations via [5]

$$X_{CH_4} = \frac{[CO]_{out} + [CO_2]_{out}}{[CH_4]_{out} + [CO]_{out} + [CO_2]_{out}} \quad (1)$$

The forward CH_4 turnover rates (r_f) were calculated by correction of the measured net reaction rate (r_n) for the approach to thermodynamic equilibrium (η) [10] using

$$r_f = \frac{r_n}{(1-\eta)} \quad (2)$$

with $\eta = \frac{[P_{CO}][P_{H_2}]^3}{[P_{CH_4}][P_{H_2O}]}\frac{1}{K_{eq}}$

P_i the pressure of species i (bar) and K_{eq} the equilibrium constant of the SMR reaction, which amounts to 9.54×10^{-3} at 500 °C (5.87×10^{-3} at 400 °C). These corrections were very minor with typical initial values of η below 0.03. The rate of CH_4 consumption in the reactor was determined based on the CH_4 inlet flow. Finally, the rate for reforming is described by

$$r_f = k(T)P_{CH_4} \quad (3)$$

2.4.1. Characterization spent catalysts

Temperature-programmed oxidation (TPO) was employed to quantify the amount of carbonaceous deposits built up during the SMR reaction. After a short purging period in He, the reactor was closed and rapidly cooled to room temperature. The reactor was transported to a setup suitable for TPO experiments. TPO was carried out by heating the sample at a rate of 10 °C/min to 750 °C in a flow of 6 vol.% O_2 in He. The amount of CO_2 was determined by online mass spectrometry (quadrupole mass spectrometer, Balzers TPG-300). The CO_2 signal was calibrated by following the decomposition of a well-known amount of $NaHCO_3$ (Acros, purity >99.5%). In a separate set of experiments, the reduced catalyst was exposed to a feed consisting of 10 vol.% CH_4 in He at a temperature of 500 °C, purged in He and cooled to room temperature, followed by a similar TPO experiment. For X-ray absorption spectroscopy of spent samples, an amount of catalyst was exposed to SMR conditions for 75 h, purged in He and rapidly cooled to room temperature and transferred under exclusion of air to a nitrogen-flushed glove box. The samples were brought to the synchrotron facility (ESRF) and loaded into the XAS cell under exclusion of air.

3. Results

3.1. Characterization

3.1.1. Textural properties and metal loading

Table 1 lists the textural properties of the various support materials before and after further calcination. The precursors were calcined at various temperatures in the range 350–900 °C in order to modify the textural properties and the final Rh particle size [34–36]. The zirconia supports contained mainly the monoclinic phase with minor amounts of the tetragonal phase. After calcination of the cerium carbonate hydroxide precursor, ceria was obtained and indexed as the *fcc* fluorite phase with space group *Fm*3*m*. This form of ceria has a polycrystalline nature. As the reducibility and reactivity of the various surface planes of ceria have a pronounced effect on the catalytic activity of the active metal phase [37], ceria nanorods and nanocubes were prepared as well. The morphology of these nanostructured materials by TEM (not shown) is similar to that reported before [30,38]. The lattice parameter of the ceria nanocubes (a = 5.406 Å), which is equal to that of the CeO_2 supports, is different from the value of 5.420 Å found for the nanorods. This lattice distortion is caused by the presence of Ce^{3+} ions in the lattice (Ce^{3+}: r = 1.14 Å; Ce^{4+}: r = 0.97 Å) [39,40] and is indicative of the higher reducibility of this form of ceria. The ceria nanorods have a typical width of 6.5 ± 1.6 nm and lengths in the range 30–200 nm. The ceria nanocubes have a quite broad size distribution ranging from 10 to 100 nm. The XRD patterns (not shown) of the calcined $CeZrO_2$ supports indicate that they exhibit the tetragonal phase [41]. In comparison with *t*-ZrO_2, the (1 1 1) peak shifted down from 2θ = 30.3° to 29.8° because of replacement of Zr^{4+} (0.84 Å) with the larger Ce^{4+} ion (0.97 Å) [42]. No diffraction peaks assigned to ZrO_2 or CeO_2 as segregated phases were detected irrespective of the calcination temperature. The lattice parameter (a) is 5.180 Å, in agreement with values found for solid solutions of similar composition [43].

Table 2 lists the most important properties of the catalysts prepared in the present study. Only ageing treatments at elevated temperature affected the textural properties after introduction of the metal. Ageing led to a decrease in the metal loading for the SiO_2-supported catalyst but not for the others catalysts.

3.1.2. Metal dispersion

H_2-chemisorption and TEM were employed to determine the metal dispersion of reduced catalysts. H_2-chemisorption measurements were performed at −80 °C to suppress hydrogen spillover to the reducible support [44,45].

The metal dispersion and the corresponding estimated particle size of the Rh/ZrO_2 and Rh/CeO_2 catalysts are given in Table 3. Figs. 2 and 3 show representative transmission electron micrographs and the corresponding particle size distributions. It was difficult to determine the particle size accurately for highly dispersed catalysts due to the small difference in contrast between rhodium and the support materials. The smallest particles that could be observed in the electron micrographs of Rh/CeO_2 were around 2 nm. For highly dispersed catalysts, the dispersion was determined by H_2-chemisorption. To validate that this approach did not introduce systematic errors, the dispersion from chemisorption and electron microscopy was compared for some samples and found to be in satisfactory agreement. The average Rh particle size was varied between 1.4 and 9 nm and 1.3 and 7.8 nm for ZrO_2- and CeO_2-supported catalysts, respectively. The initially narrow particle size distributions broaden as a result of ageing at high temperature. The metal dispersion in CeO_2-rod-supported Rh was much higher in the CeO_2-cube-supported one.

The dispersion results of the $Rh/CeZrO_2$ and Rh/SiO_2 catalysts are collected in Table 4. Several representative electron micrographs are given in Fig. 4. The trends of the dispersion as a function of the Rh loading and the support are similar as noted for the other catalysts. The dispersion of the $CeZrO_2$-catalysts is

Table 3
Metal dispersion of reduced Rh/ZrO_2 and Rh/CeO_2 catalysts.

Catalyst	H_2-chemisorption		TEM	
	d_{av}[a] (nm)	D[b] (%)	d_{av} (nm)	D (%)
Rh(0.1, 600)/ZrO_2(600)	1.4	79	–	–
Rh(0.4, 600)/ZrO_2(600)	1.4	77	–	–
Rh(0.8, 600)/ZrO_2(600)	1.6	69	–	–
Rh(1.6, 600)/ZrO_2(600)	2.3	47	–	–
Rh(0.4, 600)/ZrO_2(900)	4.2	26	–	–
Rh(1.6, 600)/ZrO_2(900)	4.7	23	4.5 ± 1.5	24
Rh(1.6, 900)/ZrO_2(900)	–	–	*n.d.*	–
Rh(1.6, a750)/ZrO_2(900)	–	–	4.7 ± 1.5	23
Rh(1.6, a900)/ZrO_2(900)	7.0	16	6.6 ± 3	17
Rh(1.6, a1000)/ZrO_2(900)	–	–	9.0 ± 2.5	12
Rh(0.1, 550)/CeO_2(550)	1.3	83	–	–
Rh(0.4, 550)/CeO_2(550)	1.6	69	–	–
Rh(0.8, 550)/CeO_2(550)	2.1	51	–	–
Rh(1.6, 550)/CeO_2(550)	2.8	39	–	–
Rh(0.4, 550)/CeO_2(900)	3.8	29	–	–
Rh(1.6, 550)/CeO_2(900)	–	–	5.2 ± 1.9	21
Rh(1.6, 900)/CeO_2(900)	–	–	6.3 ± 1.6	17
Rh(1.6, a750)/CeO_2(900)	–	–	*n.d.*	–
Rh(1.6, a900)/CeO_2(900)	–	–	7.2 ± 5	15
Rh(1.6, a1000)/CeO_2(900)	–	–	7.8 ± 2.5	14
Rh(0.1, 500)/CeO_2-rod(500)	1.2	91	–	–
Rh(1.6, 500)/CeO_2-rod(500)	1.4	78	–	–
Rh(1.6, 500)/CeO_2-cube(500)	2.3	48	–	–

[a] Average particle size.
[b] Dispersion.

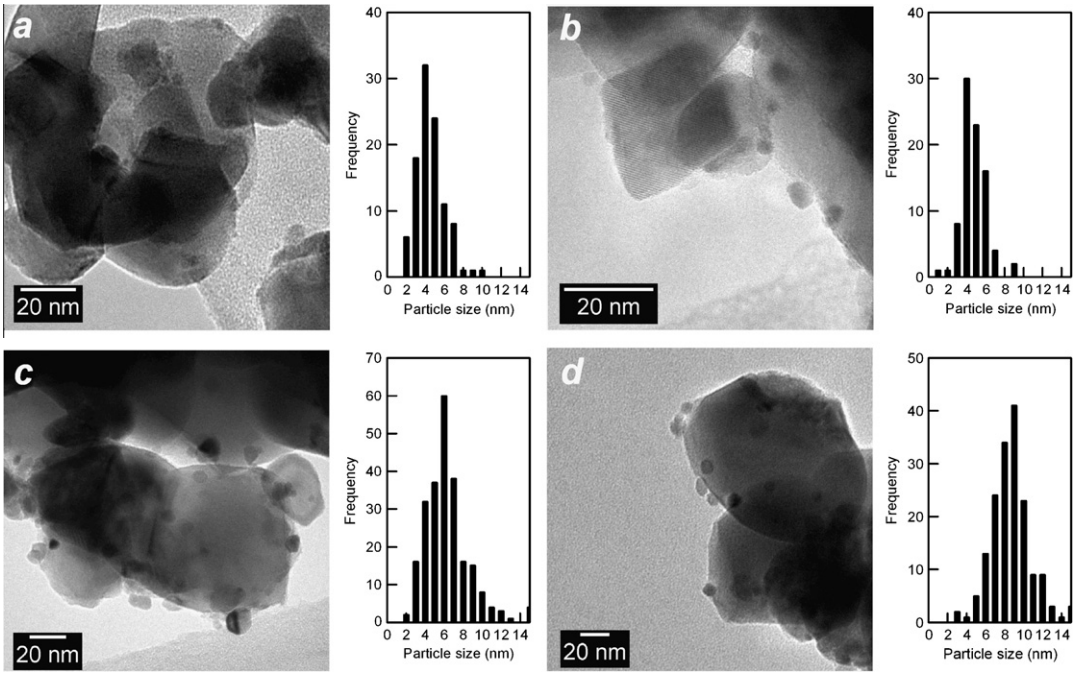

Fig. 2. Transmission electron micrographs and rhodium particle size distributions of (a) Rh(1.6, 600)/ZrO_2(900), (b) Rh(1.6, a750)/ZrO_2(900), (c) Rh(1.6, a900)/ZrO_2(900), and (d) Rh(1.6, a1000)/ZrO_2(900) with average particle diameters 4.5, 4.7, 6.6 and 9 nm, respectively.

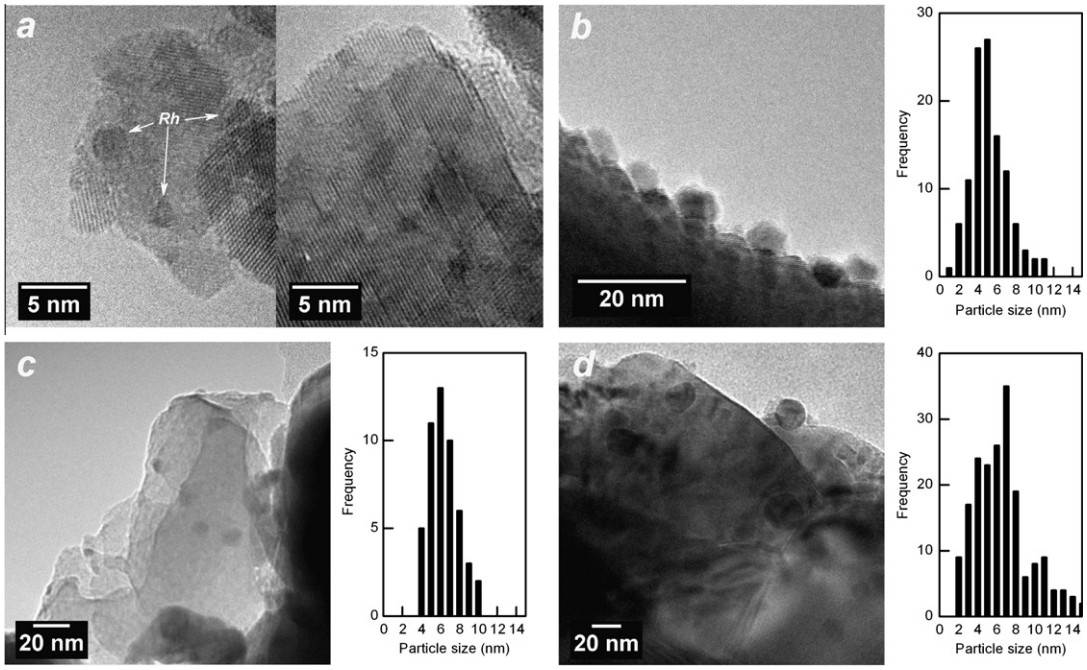

Fig. 3. Transmission electron micrographs and rhodium particle size distributions of (a) Rh(1.6, 550)/CeO_2(550), (b) Rh(1.6, 550)/CeO_2(900), (c) Rh(1.6, 900)/CeO_2(900), and (d) Rh(1.6, a900)/CeO_2(900) with average particle diameters 2–3.5, 5.2, 6.3 and 7.2 nm, respectively.

typically somewhat higher than that of the ZrO_2- and CeO_2-supported catalysts. The dispersion of the Rh/SiO_2 catalysts was only determined by TEM.

3.1.3. Reducibility of the active phase

Figs. 5 and 6 show Rh K-near-edge spectra during the reduction of a representative set of Rh/ZrO_2 and Rh/CeO_2 catalysts. Fig. 5 includes reference spectra of metallic Rh and Rh_2O_3. The whiteline of the oxidic precursor is substantially higher than for the metal due to the lower occupancy of *d*-orbitals. The changes in the near-edge spectra evidence the reduction of the rhodium oxide precursor to metallic Rh. The near-edge region of the calcined catalysts is similar to that of the rhodium oxide reference material. Reduction at 100 °C did not lead to any significant changes. The spectra after reduction at 200 °C have pronouncedly changed. A clear shift of the edge to lower energies is observed and the whiteline feature has decreased, which means that reduction has taken place. Reduction at higher temperatures only results in minor changes in the

Table 4
Metal dispersion of reduced Rh/$CeZrO_2$ and Rh/SiO_2 catalysts.

Catalyst	H_2-chemisorption		TEM	
	d_{av} (nm)	D (%)	d_{av} (nm)	D (%)
Rh(0.1, 600)/$CeZrO_2$(600)	1.1	97	–	–
Rh(0.4, 600)/$CeZrO_2$(600)	1.4	77	–	–
Rh(0.8, 600)/$CeZrO_2$(600)	1.5	72	–	–
Rh(1.6, 600)/$CeZrO_2$(600)	1.6	69	–	–
Rh(0.4, 600)/$CeZrO_2$(900)	3.5	31	–	–
Rh(1.6, 600)/$CeZrO_2$(900)	–	–	3.7 ± 1	30
Rh(1.6, 900)/$CeZrO_2$(900)	–	–	*n.d.*	–
Rh(1.6, a900)/$CeZrO_2$(900)	–	–	4.6 ± 1.2	24
Rh(1.6, a1000)/$CeZrO_2$(900)	–	–	*n.d.*	–
Rh(0.1, 550)/SiO_2	–	–	*n.d.*	–
Rh(0.4, 550)/SiO_2	–	–	2.4 ± 0.5	46
Rh(0.8, 550)/SiO_2	–	–	2.5 ± 0.4	44
Rh(1.6, 550)/SiO_2	–	–	2.9 ± 0.7	38
Rh(0.8, 550)/SiO_2(900)	–	–	*n.d.*	–
Rh(1.6, 550)/SiO_2(900)	–	–	3.3 ± 1	33
Rh(1.6, 900)/SiO_2(900)	–	–	4.7 ± 2.5	23
Rh(1.6, a750)/SiO_2(900)	–	–	6.2 ± 3	18
Rh(1.6, a900)/SiO_2(900)	–	–	8.0 ± 3.5	14

XANES spectra. This means that reduction mainly occurs in the temperature range 100–200 °C.

Fig. 6 shows similar spectra for three Rh/CeO_2 catalysts with small (D = 83%), medium (D = 39%) and large (D = 15%) average metal particle size. Reduction at room temperature and 100 °C does not result in spectral changes for Rh(0.1, 550)/CeO_2(550) and Rh(1.6, 550)/CeO_2(550). Reduction commences at 200 °C and is more pronounced for Rh(1.6, 550)/CeO_2(550) than for Rh(0.1, 550)/CeO_2(550). With increasing temperature, these two catalysts become more reduced. Clearly, reduction of Rh(0.1, 550)/CeO_2(550) is not complete. The Rh(1.6, a900)/CeO_2(900) catalyst shows a completely different behaviour. The room temperature spectrum shares features with the Rh foil, indicating the metallic character of Rh. The changes in the near-edge spectra upon further reduction are minor for this catalyst.

To quantify the differences in reduction degree of the reduced catalysts, the near-edge spectra were fitted by linear combinations of the near-edge spectra of the Rh foil and Rh_2O_3. An overview of the fraction of oxidic Rh (f_{Rh3+}) is given in Table 5. These data confirm that reduction takes mainly place between 100 and 200 °C. An exception to this are the aged catalysts, which clearly have already been reduced substantially during the ageing treatment.

Fig. 7 relates the reduction degree to the Rh particle size after reduction at 400 and 500 °C. The differences in the reduction degree between these two reduction temperatures are very small. The reducibility depends on the average particle size. When the particles become smaller than 4 nm, they become increasingly more difficult to reduce. Particles larger than about 4 nm are nearly fully reduced (f_{Rh3+} <10%). Clearly, the reduction degree of the CeO_2-supported catalysts is lower than that of the $CeZrO_2$-, ZrO_2- and SiO_2-supported ones and this difference should be due to the strong metal–ceria interactions [46–49].

Fig. 8 shows the experimental and fitted k^3-weighted $\chi(k)$ EXAFS functions and the corresponding Fourier Transforms (FT) of a set conventional CeO_2-supported catalysts after reduction. The fit parameters are given in Table 6. In general, the FT spectra can be fitted by a Rh-O shell at 2.06 Å and a Rh-Rh shell around 2.69 Å. Higher Rh-Rh shells similar to those observed for the metallic Rh foil were not used in the fitting procedure but are clearly present when the Rh particles are large. Small Rh particles (d_{av} < ~2 nm) contain a Rh–Rh shell at a coordination distance (R) slightly lower than 2.69 Å and a coordination number (N) between 4 and 7. The small Rh–Rh bond length contraction appears to be independent of the type of support. A shorter interatomic bond length favours enhanced d–d interactions, which narrows the d-band and lowers the energy of the d-orbitals. Accordingly, a lower intensity of the whiteline in the edge region of the X-ray absorption spectra is observed (not shown). Similar effects have been reported before for both Pt and Au catalysts [50]. The spectra also contain a contribution of an oxygen back-scatterer, which is due to the presence of a small fraction of Rh-oxide particles that cannot be reduced. Such a Rh–oxide shell is absent in the spectra of larger Rh particles. With increasing Rh particle size, the coordination number increases to values close to the bulk value of 12, while the Rh–Rh bond distance remains at 2.69 Å.

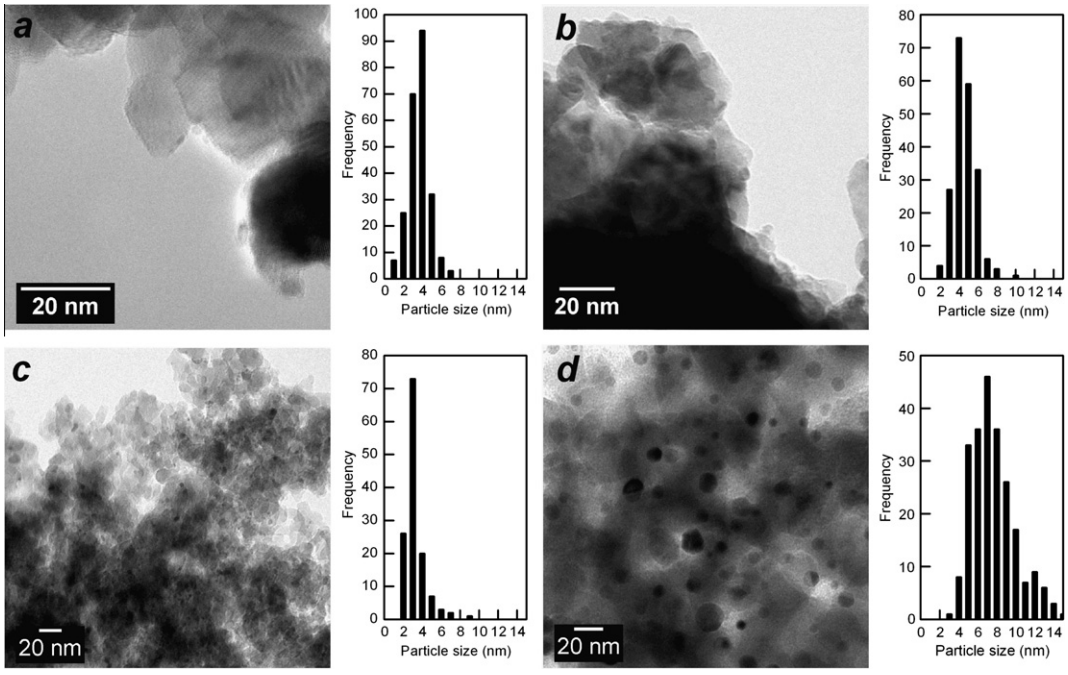

Fig. 4. Transmission electron micrographs and rhodium particle size distributions of (a) Rh(1.6, 600)/$CeZrO_2$(900), (b) Rh(1.6, a900)/$CeZrO_2$(900), (c) Rh(1.6, 550)/SiO_2(900), and (d) Rh(1.6, a900)/SiO_2(900) with average particle diameters 3.7, 4.6, 3.3 and 8.0 nm, respectively.

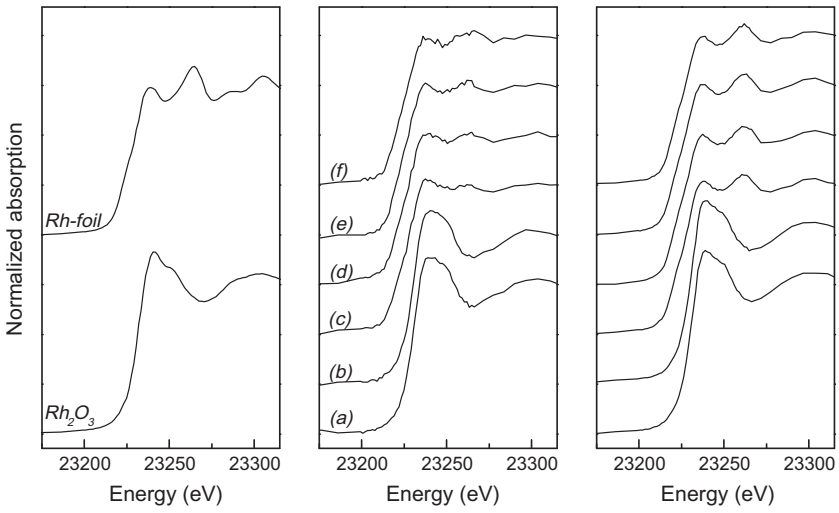

Fig. 5. Rh *K*-edge XANES spectra recorded of (left) references: Rh_2O_3 and Rh foil, (middle) Rh(0.5, 600)/ZrO_2(600) and (right) Rh(1.6, 600)/ZrO_2(600) during reduction at (a) room temperature, (b) 100 °C, (c) 200 °C, (d) 300 °C, (e) 400 °C and (f) 500 °C.

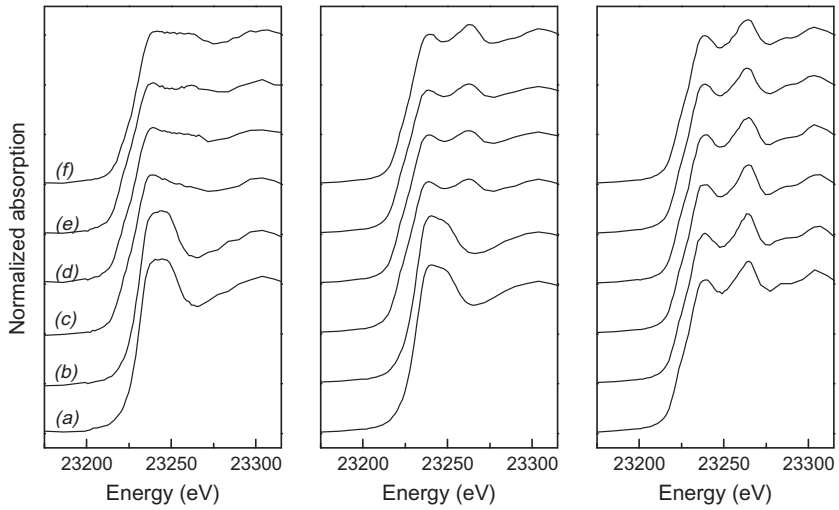

Fig. 6. Rh *K*-edge XANES spectra recorded of (left) Rh(0.1, 550)/CeO_2(550), (middle) Rh(1.6, 550)/CeO_2(550) and (right) Rh(1.6, a900)/CeO_2(900) during reduction at (a) room temperature, (b) 100 °C, (c) 200 °C, (d) 300 °C, (e) 400 °C and (f) 500 °C.

Fig. 9 relates the Rh–Rh coordination number to the Rh particle size for a larger set of catalysts. The data are fitted with a simple logarithmic function, which can be used to derive the average metal particle size ($d_{average}$) from the coordination number of the first Rh–Rh shell (N_{Rh-Rh}) by

$$N_{Rh-Rh} = 3.815 \cdot \ln(d_{av}) + 3.88 \quad (4)$$

Additional data from the literature fit this correlation well. For subnanometer-sized Rh particles, the estimation of the average particle size from the Rh-Rh coordination number [59–62] has often been based on the work of Van Zon et al. [51]. The particle sizes are a bit lower than the correlation due to assumptions in applying chemisorption [63]. The empirical function can be extended to metals of similar structure [50].

3.2. Catalytic activity measurements

3.2.1. Catalytic activity and stability

A large number of catalysts were tested for their activity in the steam methane reforming reaction. The catalysts displayed considerable differences in their activities and stabilities as a function of time on stream. As a representative example, Fig. 10 shows the surface-atom-based activity of three ZrO_2-supported catalysts with low, medium and high metal dispersion as a function of time on stream. The initial intrinsic activity decreases with increasing Rh particle size. Despite the much higher initial activity of the catalyst with the highest Rh dispersion, deactivation is much more pronounced than for the other two catalysts. The catalyst containing the largest Rh particles exhibits stable activity in the SMR reaction.

Table 7 lists the weight-based and surface-atom-based reaction rates of methane after 0.5 h and 15 h. The weight-based initial activities show an optimum in the dispersion range of 50–70%. It is however more useful in the light of our discussion to compare the surface-atom-based reaction rates. In doing so, it is observed that the initial intrinsic activity increases with the Rh dispersion for a set of catalysts on a particular support. It is also noteworthy that the initial intrinsic reaction rates do not vary significantly between catalysts based on different supports and with similar dispersion. For instance, the initial reaction rates of CeO_2-, ZrO_2- and $CeZrO_2$-supported catalysts with Rh dispersion close to 69% are very similar. Another important conclusion is that all catalysts containing Rh particles smaller than about 3 nm deactivate. Cata-

Table 5
Rh *K*-edge XANES spectra fitting results: fraction of oxidic Rh (f_{Rh3+}) of supported catalysts during reduction from room temperature to 500 °C.

Catalyst	*D* (%)	f_{Rh3+} (%)					
		RT	100 °C	200 °C	300 °C	400 °C	500 °C
Rh(0.1, 600)/ZrO_2(600)	79	100	100	42	36	33	31
Rh(0.4, 600)/ZrO_2(600)	77	100	97	36	23	20	19
Rh(0.8, 600)/ZrO_2(600)	69	100	83	35	22	19	17
Rh(1.6, 600)/ZrO_2(600)	47	100	94	21	17	13	12
Rh(0.1, 550)/CeO_2(550)	83	100	100	55	50	47	34
Rh(0.4, 550)/CeO_2(550)	69	100	99	52	46	39	29
Rh(0.8, 550)/CeO_2(550)	51	100	–	33	32	26	22
Rh(1.6, 550)/CeO_2(550)	39	100	96	27	24	21	19
Rh(1.6, 550)/CeO_2(900)	21	94	88	14	11	7	8
Rh(1.6, a900)/CeO_2(900)	15	18	3	3	5	5	7
Rh(1.6, 500)/CeO_2-rod(500)	78	100	100	27	24	21	20
Rh(1.6, 500)/CeO_2-cube(500)	48	100	27	18	17	15	14
Rh(0.1, 600)/$CeZrO_2$(600)	97	100	100	87	63	40	32
Rh(0.4, 600)/$CeZrO_2$(600)	77	100	97	82	57	35	28
Rh(0.8, 600)/$CeZrO_2$(600)	72	100	89	53	35	30	21
Rh(1.6, 600)/$CeZrO_2$(600)	69	100	–	25	20	17	15
Rh(1.6, 600)/$CeZrO_2$(900)	30	–	–	–	–	–	10
Rh(1.6, a900)/$CeZrO_2$(900)	24	5	–	–	–	–	6
Rh(1.6, 550)/SiO_2	38	95	68	17	15	12	9
Rh(1.6, a900)/SiO_2(900)	14	10	–	–	–	–	6

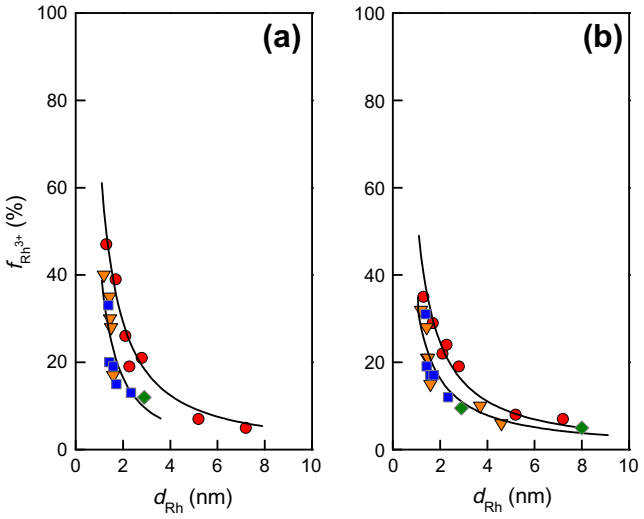

Fig. 7. Fraction of oxidic Rh (f_{Rh3+}) as a function of Rh particle size supported by CeO_2 (circles), $CeZrO_2$ (triangles), ZrO_2 (squares) and SiO_2 (rhombi) during reduction at (a) 400 °C and (b) 500 °C.

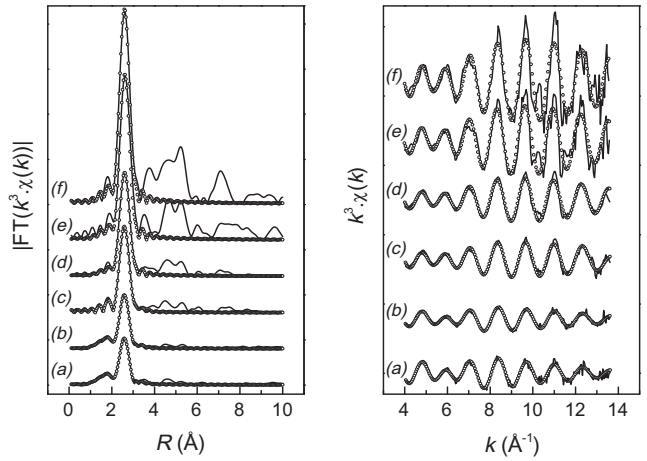

Fig. 8. Experimental (solid line) and fitted (dotted points) (left) FT EXAFS functions and (right) k^3-weighted EXAFS oscillations of (a) Rh(0.1, 550)/CeO_2(550), (b) Rh(0.4, 550)/CeO_2(550), (c) Rh(0.8, 550)/CeO_2(550), (d) Rh(1.6, 550)/CeO_2(550), (e) Rh(1.6, 550)/CeO_2(900) and (f) Rh(1.6, a900)/CeO_2(900) after reduction.

lysts containing larger nanoparticles exhibit a quite stable SMR activity.

The approach of the reaction toward the water–gas shift equilibrium is also included in Table 7. These values were determined from the concentrations of reactants and products as defined by

$$\eta_{WGS} = \frac{[P_{CO_2}][P_{H_2}]}{[P_{CO}][P_{H_2O}]}\frac{1}{K_{eq,WGS}}, \quad (5)$$

with $K_{eq,WGS}$ amounting to 5.03 at 500 °C.

WGS reaction rates are generally considered to be sufficiently high to obtain the WGS equilibrium [10,64]. Although this may be true at high reaction temperatures, the present data obtained at 500 °C show that η_{WGS} considerably depends on the particle size and the type of support. The WGS activity is highest for Rh particles supported by ceria. Catalysts containing small Rh particles ($D > \sim 30\%$) show decreasing WGS activity with the type of support in the order $CeO_2 > CeZrO_2 > ZrO_2 > SiO_2$. Catalysts that contain large Rh particles ($D < \sim 20\%$) have much lower WGS activities than catalysts containing small Rh particles.

3.2.2. Characterization of spent catalysts

Table 8 collects the amount of carbon deposited during SMR and exposure to CH_4/He at 500 °C. Clearly, the total amount of coke built up during SMR depends only slightly on the dispersion of the catalyst. The ratio of carbon to surface metal atoms, however, is higher than unity and increases with the dispersion. The experiments as a function of time on stream for Rh(0.1, 600)/ZrO_2(600) evidence that the carbonaceous deposits built up progressively with time on stream. Therefore, the coke is not related to the deactivation of a certain amount of highly active surface sites. The amount of coke deposited during 15 h of SMR is relatively smaller than the amount built up during the exposure to CH_4/He at the same temperature for 10 min. For the latter type of experiments, a maximum amount of coke is found for intermediate particle size. This is to be contrasted to the much smaller variation in coke formation following SMR.

Table 6
Fit parameters of k^3-weighted EXAFS spectra at the Rh *K*-edge of supported catalysts after reduction and reaction.

Catalyst	Treatment	f_{Rh3+}[a] (%)	EXAFS analysis[b]				
			Shell	R (Å)	N	$\Delta\sigma^2$ (Å^2)	E_0 (eV)
Rh(0.1, 550)/CeO_2(550)	H_2, 500 °C	28	Rh-O	2.06	0.9	0.004	−6.0
			Rh-Rh	2.65	4.3	0.012	
	Spent[c]	65	Rh-O	2.05	3.0	0.006	2.3
			Rh-Rh	2.66	2.7	0.009	
Rh(0.4, 550)/CeO_2(550)	H_2, 500 °C	27	Rh-O	2.05	1.3	0.008	4.7
			Rh-Rh	2.67	5.2	0.009	
Rh(0.8, 550)/CeO_2(550)	H_2, 500 °C	24	Rh-O	2.03	0.5	0.003	5.2
			Rh-Rh	2.68	5.7	0.007	
Rh(1.6, 550)/CeO_2(550)	H_2, 500 °C	19	Rh-Rh	2.69	6.6	0.006	3.6
	Spent[c]	39	Rh-O	2.06	2.1	0.008	3.3
			Rh-Rh	2.68	4.5	0.007	
Rh(1.6, 550)/CeO_2(900)	H_2, 500 °C	10	Rh-Rh	2.69	10.1	0.006	3.0
Rh(1.6, a900)/CeO_2(900)	H_2, 500 °C	2	Rh-Rh	2.69	11.8	0.006	3.4
	Spent[c]	3	Rh-Rh	2.69	9.8	0.005	4.0
Rh(1.6, 500)/CeO_2-rod(500)	H_2, 500 °C	21	Rh-Rh	2.68	5.9	0.007	2.8
Rh(1.6, 500)/CeO_2-cube(500)	H_2, 500 °C	15	Rh-Rh	2.69	8.1	0.005	2.4
Rh(0.8, 600)/$CeZrO_2$(600)	H_2, 500 °C	18	Rh-O	2.06	1.4	0.015	1.3
			Rh-Rh	2.68	4.6	0.007	
Rh(1.6, 600)/$CeZrO_2$(600)	H_2, 500 °C	13	Rh-Rh	2.68	6.5	0.007	1.1
Rh(0.8, 600)/ZrO_2(600)	H_2, 500 °C	19	Rh-Rh	2.66	4.7	0.006	7.2
Rh(1.6, 600)/ZrO_2(600)	H_2, 500 °C	13	Rh-Rh	2.68	8.5	0.007	3.0
Rh(1.6, 550)/SiO_2	H_2, 500 °C	10	Rh-Rh	2.68	7.5	0.006	4.5

[a] Fitting of near-edge spectra.
[b] Only Rh–O and Rh–Rh shells fitted; Δk = 2.5–13.4 Å^{-1}; estimated error in R ± 0.01 Å, N ± 20%, $\Delta\sigma^2$ ± 10%.
[c] SMR for 75 h at 500 °C in 0.06 bar CH_4 and 0.18 bar H_2O.

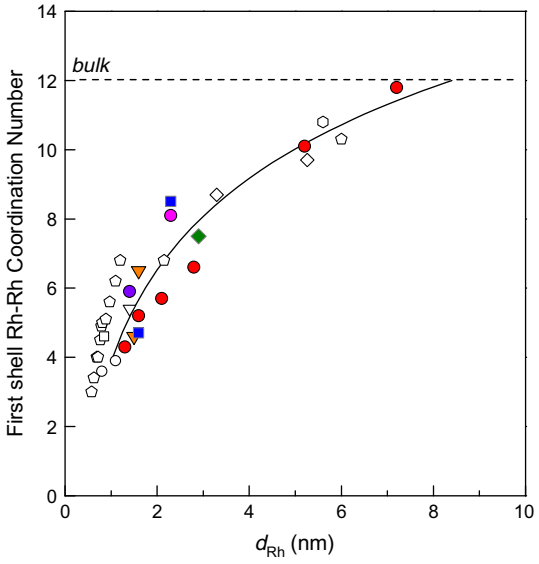

Fig. 9. First shell Rh-Rh coordination number as a function of the Rh diameter on CeO_2 (circles), $CeZrO_2$ (triangles), ZrO_2 (squares) and SiO_2 (rhombi). Our particle sizes (closed symbols) were determined by H_2-chemisorption and TEM analysis. Literature results for Rh/Al_2O_3 (pentagons) [51–53], Rh/CeO_2 [54], Rh/$CeZrO_2$ [55], Rh/ZrO_2 [56], Rh/SiO_2 [57] and Rh/MgO (hexagon) [58] are included for comparison.

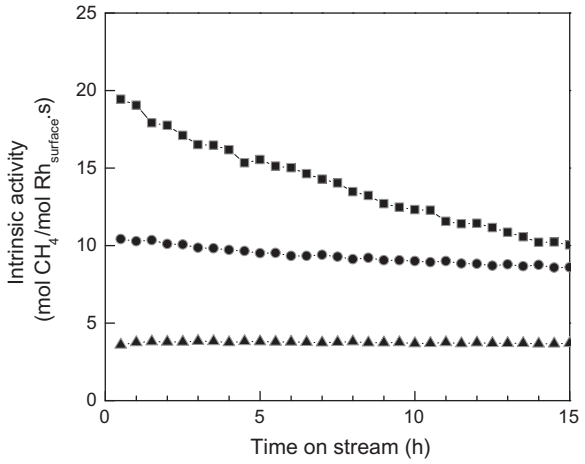

Fig. 10. CH_4 steam reforming rates as functions of time on stream of (squares) Rh(0.1, 600)/ZrO_2(600), (circles) Rh(1.6, 600)/ZrO_2(600) and (triangles) Rh(1.6, a900)/ZrO_2(900) (500 °C, 0.06 bar CH_4, 0.18 bar H_2O).

Table 6 contains the fit parameters of the Fourier-transformed k^3-weighted EXAFS functions of spent CeO_2-supported catalysts with initial metal dispersions of 83%, 39% and 15% after reduction. The corresponding Fourier transforms and EXAFS functions are shown in Fig. 11. Compared to the freshly reduced catalysts, the FT function of spent Rh(0.1, 550)/CeO_2(550) contains a much smaller contribution of the Rh-Rh shell. The coordination number has decreased from 4.3 to 2.7. At the same time, the Rh–O coordination number, which was only 0.9 in the reduced catalyst, increased to 3.0. These results suggest that the very small particles have not sintered during the SMR reaction but instead have oxidized. In support of this is the analysis of the near-edge spectra, which shows an increase of the fraction of oxidic Rh from 28% to 65%. The Rh(1.6, 550)/CeO_2(550) catalyst, which contains Rh particles with an average size of 2.8 nm, deactivates less pronouncedly than Rh(0.1, 550)/CeO_2(550). The coordination number of the Rh–Rh shell is 6.6 for the freshly reduced catalyst and decreases to 4.5. Concomitantly, the Rh–O shell increases pointing to partial oxidation of this catalyst. The degree of oxidation of this catalyst is lower than for the very small particles in Rh(0.1, 550)/CeO_2(550). Finally, Rh(1.6, a900)/CeO_2(900) initially contains 7.2 nm Rh particles with a Rh-Rh coordination number of 11.8. After SMR, the coordination number only changed slightly to 9.8. Most importantly, we observed that the Rh particles remain nearly completely reduced.

Table 7
CH_4 steam reforming rates[a] initial and 15 h on stream of a selected set of catalysts (500 °C, 0.06 bar CH_4, 0.18 bar H_2O), and the extent of water–gas shift equilibrium (η_{WGS}).

Catalyst	D (%)	$r_{initial}$		r_{15h}		η_{WGS} (−)
		(mol/g_{cat}·h)	(mol/mol Rh_{surf}·s)	(mol/g_{cat}·h)	(mol/mol Rh_{surf}·s)	
Rh(0.1, 600)/ZrO_2(600)	79	0.43	14	0.14	4.7	0.55
Rh(0.4, 600)/ZrO_2(600)	77	1.66	13.7	1.17	9.6	0.45
Rh(0.8, 600)/ZrO_2(600)	69	2.52	12.9	2.21	11.2	0.68
Rh(1.6, 600)/ZrO_2(600)	47	2.33	8.8	1.95	7.3	0.6
Rh(1.6, 600)/ZrO_2(900)	24	0.71	5.4	0.69	5.3	0.56
Rh(1.6, a750)/ZrO_2(900)	23	0.64	5	0.66	5.3	0.2
Rh(1.6, a900)/ZrO_2(900)	17	0.35	3.6	0.34	3.5	0.02
Rh(1.6, a1000)/ZrO_2(900)	12	0.19	2.6	0.18	2.4	0.01
Rh(0.1, 550)/CeO_2(550)	83	0.41	9.3	0.13	3	1
Rh(0.4, 550)/CeO_2(550)	69	1.33	10.6	0.88	7	0.91
Rh(0.8, 550)/CeO_2(550)	51	1.97	11.3	1.58	9.1	0.97
Rh(1.6, 550)/CeO_2(550)	39	2.62	10	2.46	9.4	0.98
Rh(1.6, 550)/CeO_2(900)	21	0.63	5.5	0.6	5.2	0.82
Rh(1.6, a900)/CeO_2(900)	15	0.08	1	0.03	0.4	0.03
Rh(1.6, 500)/CeO_2-rod(500)	78	0.38	13.2	0.33	11.4	0.92
Rh(1.6, 500)/CeO_2-cube(500)	48	2.43	9.2	2.28	8.6	0.8
Rh(1.6, 600)/$CeZrO_2$(600)	69	2.3	11.5	2.17	10.8	0.85
Rh(1.6, a900)/$CeZrO_2$(900)	24	0.45	3.1	0.41	2.9	0.22
Rh(1.6, 550)/SiO_2(900)	33	1.24	6.8	1.03	5.7	0.18
Rh(1.6, a750)/SiO_2(900)	14	0.12	1.6	0.11	1.5	0.03

[a] $r_{initial}$ (r_{15h}) is defined as the average rate between 0.5 and 2.5 h (15 and 17 h).

Table 8
The amount of carbon in spent Rh/ZrO_2 and Rh/CeO_2 catalysts after SMR and exposure to CH_4/He as determined by TPO.

Catalyst	D (%)	t [a](h)	P_{CH4} (bar)	P_{H2O} (bar)	T_{max} (°C)	Coke (mmol/g_{cat})	Coke (mmol/mmol Rh_{surf})
Rh(0.1, 600)/ZrO_2(600)	79	2.5	0.06	0.18	271	0.12	13.7
		8.5	0.06	0.18	285	0.3	35.8
		15	0.06	0.18	319	0.57	67.4
		0.167	0.1	0.18	307	0.06	7.0
Rh(1.6, 600)/ZrO_2(600)	47	15	0.06	0	276	0.23	3.2
		0.167	0.1	0	320	1.21	16.3
Rh(1.6, 600)/ZrO_2(900)	24	15	0.06	0.18	285	0.36	9.5
		0.167	0.1	0	322	0.26	6.8
Rh(1.6, a900)/ZrO_2(900)	17	15	0.06	0.18	319	0.4	11.6
		0.167	0.1	0	484	0.08	3.0
Rh(0.1, 550)/CeO_2(550)	83	15	0.06	0.18	268	0.6	49.9
Rh(0.8, 550)/CeO_2(550)	51	15	0.06	0.18	260	0.33	7.2
Rh(1.6, 550)/CeO_2(900)	21	15	0.06	0.18	266	0.2	6.1
Rh(1.6, a900)/CeO_2(900)	15	15	0.06	0.18	289	0.19	8.1

[a] Time on stream.

4. Discussion

Insight into the influence of the number of particular surface sites such as terraces ($N_{terrace}$), edges (N_{edge}), corners (N_{corner}) and step edges (N_{step}) can be obtained by relating the intrinsic surface atom reaction rates to the metal dispersion. Following the work of Jones et al. [7], the total reaction rate (r_{total}) will be the sum of the individual reaction rates over the various surface sites via

$$r_{total} = N_{terrace} \times r_{terrace} + N_{edge} \times r_{edge} + N_{corner} \times r_{corner} + N_{step} \times r_{step} \quad (6)$$

As typically only the metal dispersion (D) is known, the intrinsic surface atom reaction rate ($r_{intrinsic}$) is obtained by normalizing the experimental total reaction rate to the number of surface atoms (N_{total}) via

$$r_{intrinsic} = r_{experimental}/N_{total} \quad (7)$$

with $r_{experimental}$ being the turnover frequency in mol_{CH4}/g_{cat} s and N_{total} the total number of surface sites in $mol_{Rh\text{-}surf}/g_{cat}$. How $r_{intrinsic}$ relates to the metal particle dispersion depends on the individual rates for the various surface sites. If the reaction rate is controlled by the terrace sites, $r_{intrinsic}$ does not depend on the dispersion, because $N_{terrace}/N_{total}$ does not depend on the metal particle size. If the reaction rate is limited by a reaction step taking place on the edge atoms, the rate will scale linearly with metal dispersion as N_{edge} increases inversely with the particle size. If the rate-controlling step occurs on corner atoms, the rate should correlate with D^2. Finally, one should consider the special case where CO formation on the stepped site surface topology is rate-controlling. In this case, one expects that $r_{intrinsic}$ has a maximum at around 2 nm for cubo-octahedron-shaped nanoparticles. To compute meaningful values for $r_{intrinsic}$, the experimental reaction rate is corrected for the metal dispersion as well as the fraction of metallic Rh. The latter correction is required, because the fraction of Rh atoms that cannot be reduced is significant, *viz.* for the CeO_2-supported catalysts and for the other catalysts that contain very small Rh particles.

Fig. 12 shows the initial $r_{intrinsic}$ as a function of the Rh dispersion. Two important conclusions can immediately be drawn. The first is that the intrinsic reaction rate over the reduced surface metal atoms increases linearly with the metal dispersion. This finding indicates that the overall rate is controlled by a reaction step occurring on the edge atoms of the Rh nanoparticles. The second is that the initial reaction rate per surface metal atom does not

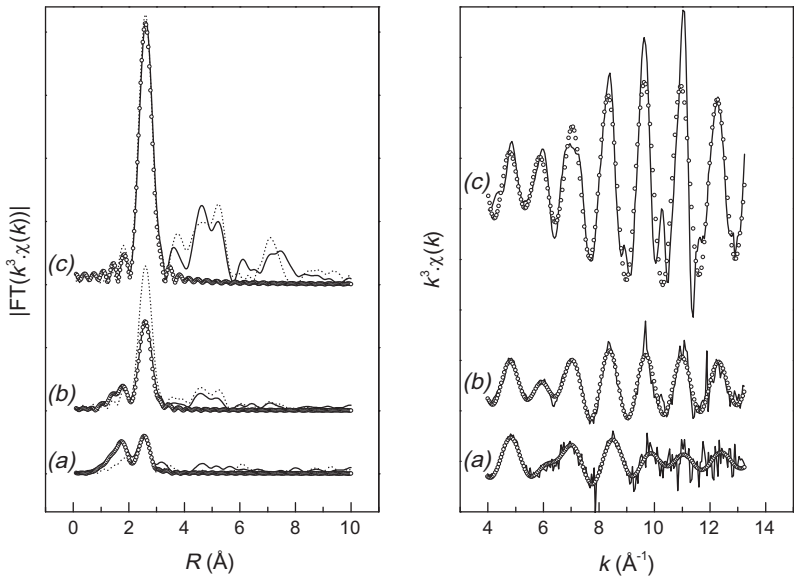

Fig. 11. Experimental (solid line) and fitted (dotted points) (left) FT EXAFS functions and (right) k^3-weighted EXAFS oscillations of (a) Rh(0.1, 550)/CeO_2(550), (b) Rh(1.6, 550)/CeO_2(550), (c) Rh(1.6, a900)/CeO_2(900) after SMR for 75 h at 500 °C in 0.06 bar CH_4 and 0.18 bar H_2O. The dotted lines are the experimental EXAFS data of the reduced catalysts.

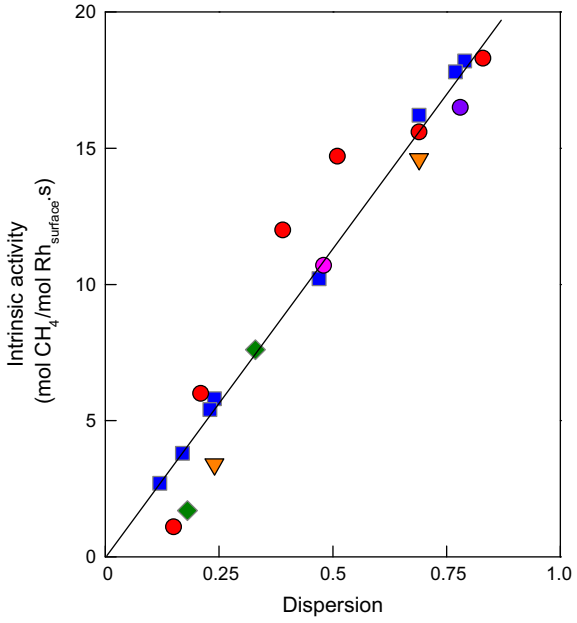

Fig. 12. Initial CH_4 steam reforming rates as function of Rh dispersion supported by ZrO_2 (squares), CeO_2-polyhedral (red circles), CeO_2-rod (purple circle), CeO_2-cube (pink circle), $CeZrO_2$ (triangles), and SiO_2 (rhombi) (500 °C, 0.06 bar CH_4, 0.18 bar H_2O).

depend on the support. These two issues will be discussed in detail below.

The linear correlation between the intrinsic reaction rate and the metal dispersion for steam methane reforming has been reported before by Jones et al. [7] and Wei and Iglesia [10]. In the work by Jones et al., a set of Rh catalysts was supported by zirconia with a varied dispersion in the range 8–32%, which implies that the smallest particles had a size of about 3 nm. This size is considerably larger than the particle size at which the density of stepped edge sites is expected to dominate on the metal nanoparticles. The smallest particle size in the present set of catalysts is 1.3 nm. The intrinsic reaction rates of our catalysts are very similar to those reported by Jones et al. [7] for similar metal dispersion. In contrast, the activities are nearly two times higher than the activities of supported Rh catalysts reported by Wei and Iglesia [10], even when the reaction temperature in the latter case was 100 °C higher. The reason for this difference is not clear, although we would like to note that we and Jones et al. use inert forms of alumina as diluent, whereas quartz powder was employed by Wei and Iglesia. As the linear relation with dispersion still holds, this allows us to extend the conclusion by Jones et al. to a much larger range of particle sizes. The data of Wei and Iglesia relate to high-temperature conditions [10], under which one expects CH_4 dissociation to be rate-controlling [23]. A word of caution is in place. The geometrical optimum of stepped edge sites of 2 nm is determined for nanoparticles with cuboctahedron morphology [17]. In reality, metal particles tend to minimize their surface energy and one way to do so is to maximize the interaction with the support. In this case, the particle shape may be different, and it is likely that stepped edge sites can still be present on very small particles that interact more strongly with the support. Indeed, the relation between the Rh-Rh coordination number and the average Rh particle size of the supported Rh catalysts in comparison with recent spectral simulation work [65] points to the presence of half-spheres in our catalysts.

The importance of surface defect sites in the activation of methane dissociation has been extensively demonstrated by periodic DFT calculations on Group VIII metals. The activation energies on Rh are typically 60 kJ/mol and higher for terrace surfaces (close-packed facets) and 30–60 kJ/mol for surface atoms with a lower metal–metal coordination number as found for edges and stepped sites [14,66]. These barriers are substantially lower than those calculated for CO formation on Rh. The activation energy for C—O recombination is ~180 kJ/mol on terrace surfaces and decreases to values on the order of 90 kJ/mol on step edge sites [23]. To meaningfully compare these barriers, one should compare the activation free energies. At a temperature of 500 °C, one has to add approximately 100 kJ/mol for the entropy loss during dissociative methane adsorption (ΔS_{act} estimated to be −130 J/mol·K), which implies a free energy activation barrier of at least 130 kJ/mol. For a surface recombination reaction, the change in entropy will be very small [67]. The free energy activation barrier for C—O recom-

bination will remain around 90 kJ/mol. This analysis predicts that the rate of dissociative methane adsorption will be lower than the rate of C—O recombination as long as step edge sites are available.

In line with earlier suggestions [1,7], this analysis implies that at sufficiently low temperatures, C—O recombination will become rate-controlling. To verify this, we determined the intrinsic rates for a number of Rh/ZrO_2 catalysts at 400 °C (Fig. 13) and found that the intrinsic rate remains linearly related to the dispersion. As in this case no catalyst deactivation was observed, a kinetic study could be carried out to determine the reaction orders in methane and steam. Fig. 14 shows that changes in the methane partial pressure range of 24 to 105 mbar did not lead to any changes in the conversion. Thus, the reaction is first-order in methane. The intrinsic activity did not depend on the steam-to-carbon ratio (S/C ratio varied between 3 and 6). Accordingly, the reaction rate equation has the form

$$r = k \cdot P_{CH_4}^{1} \cdot P_{H_2O}^{0} \tag{8}$$

similar to the form reported by Wei and Iglesia [10] for reforming at more conventional reforming temperatures of 600 °C and higher. In another set of experiments, we determined the apparent activation energy for two Rh/ZrO_2 catalysts with average particle sizes of 1.6 and 2.3 nm and found it to be 70 kJ/mol in the temperature range 330–450 °C. Wei and Iglesia [10] reported a value of 109 kJ/mol for SMR at higher temperatures for a Rh-based catalyst. Zeppieri et al. [68] found a value of 69 kJ/mol for a 5 wt.% Rh-perovskite catalyst similar to our activation energy. The present value of 70 kJ/mol is very close to theoretical values for methane activation [14,66].

Accordingly, the present experimental results allow us to conclude that (i) CH_4 dissociation is the rate-controlling step and (ii) CO formation is occurring on step edge sites. This also implies that the very small particles employed in this study still stabilize sufficient step edge sites. Jones et al. [7] assume competition between CH_4 dissociation and C—O recombination in their microkinetic model. This choice appears to be related to the relatively high barrier for C—O recombination computed for the stepped Ru(1015) surfaces, which was used to derive the barrier for Rh and other metals. A similarly high barrier on Rh for this step was found earlier by Mavrikakis et al. [69]. The free activation energy analysis then predicts competition between C—O recombination and CH_4 dissociation for the most active metals. Recently, Van Grootel et al. [23] have reported values for the activation barrier of C—O recombination for Rh(1 1 1) and Rh(2 1 1) of 180 and 90 kJ/mol, respectively, independent of whether CO forms by recombination of adsorbed C and O adatoms or via a formyl (CHO) intermediate. Obviously, this free energy analysis implies that dissociative methane adsorption will be the rate controlling step at higher reaction temperatures.

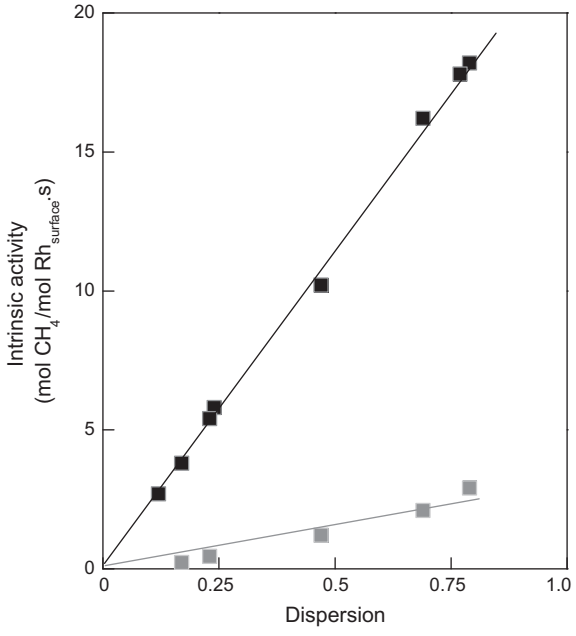

Fig. 13. Initial CH_4 steam reforming rates as function of Rh dispersion supported by ZrO_2 at 500 °C (black) and 400 °C (gray) (0.06 bar CH_4, 0.18 bar H_2O).

The other important conclusion is that the support does not influence the intrinsic reaction rate of the surface metal edge atoms. Iglesia and co-workers [10] have reached a similar conclusion by comparing the intrinsic activities of zirconia- and alumina-supported Rh catalysts. This result is in agreement with the finding that the rate is controlled by dissociative methane adsorption, because it is commonly accepted that this elementary reaction step takes place over a single metal surface atom without any involvement of the support. Several studies for supported Pt [70] and Pd [71–73] catalysts have shown a positive effect of the use of ceria in steam methane reforming. It may well be that the more difficult activation of water on Pt and Pd surfaces [23] explains the beneficial effect of ceria in such cases. Indeed, ceria and a ceria-containing support such as ceria-zirconia as employed in the present study are known to activate water, which may provide oxygen species on the metal phase via spillover [74,75].

A further interesting finding of the present work is that catalyst deactivation becomes more pronounced with decreasing Rh particle size. Deactivation is apparent for particles with an initial dispersion higher than 75%, whereas particles with dispersion between 35% and 75% deactivate less strongly. Particles larger than about 4 nm are stable in the SMR reaction. TPO of spent catalysts shows a clear relation between the amount of coke built up on the catalyst surface during SMR and the particle size. The coke is graphitic in nature as follows from the high temperature needed to hydrogenate these coke deposits [76]. The smaller the initial Rh nanoparticles, the higher the surface Rh atom normalized amount of coke in the spent catalyst. This trend is at variance with the one obtained in separate experiments involving coke deposition by exposure of the same catalysts to methane. In the presence of water (SMR reaction), C—O recombination reactions, which remove carbon from the surface, compete with carbon–carbon coupling reactions. C—O recombination occurs on stepped sites during SMR [23]. It can be expected that the density of such step edge sites decreases with a decrease in the particle size [13]. Thus, the lower density of step edge sites on small nanoparticles may result in a higher concentration of carbon (C or CH species) on the surface and, therefore, increase the rate of formation of carbonaceous deposits. Accordingly, coke deposition provides a possible explanation for the stronger catalyst deactivation of smaller Rh particles.

A detailed comparative analysis of the near-edge region and EXAFS part of the X-ray absorption spectra of reduced and spent Rh catalysts shows that very small particles are oxidized to rhodium oxide species under the SMR conditions. The smaller the initial particle size, the more extensive the oxidation of the metal phase is. This is evident from the increased fraction of oxidic Rh as well as from the increased Rh–O coordination shell. The tendency of Rh nanoparticles to become oxidized increases with decreasing the particle size [77]. We recently found that Rh nanoparticles dispersed on reducible supports with a size smaller than 2.5 nm oxidize completely and are much more active in CO oxidation than large Rh particles that remain metallic [78]. The present results also indicate that under the more reducing conditions of steam reforming, the surface oxygen atoms can oxidize these very small

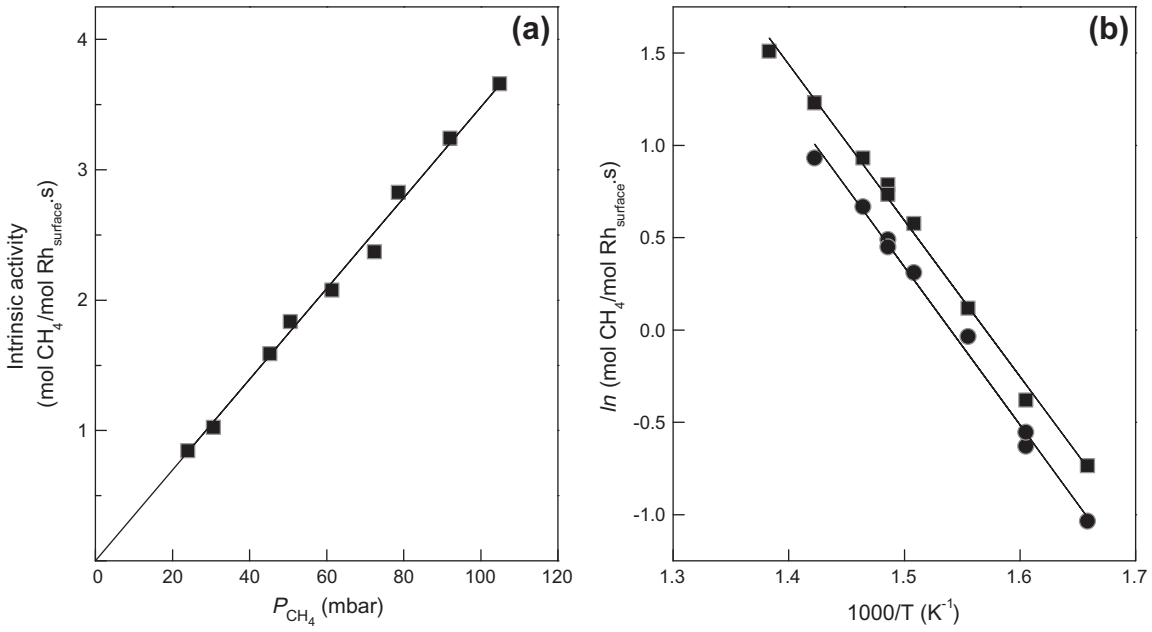

Fig. 14. Reaction kinetics for steam reforming: (a) the effect of CH_4 partial pressure on the intrinsic activity for CH_4 steam reforming of Rh(0.8, 600)/ZrO_2(600) (400 °C, total flow rate 200 ml/min, with 0.18 bar H_2O balanced by He), and (b) Arrhenius plot of Rh(0.8, 600)/ZrO_2(600) and Rh(1.6, 600)/ZrO_2(600) to give apparent activation energies of 70 ± 2 and 71 ± 3 kJ/mol, respectively.

Rh nanoparticles, whereas for CO oxidation, Rh oxide turns out to be much more active than Rh metal; this is not the case for steam methane reforming because of the necessity of activating the C–H bonds of methane over Rh surface metal atoms. Thus, oxidation of very small Rh particles provides a reasonable explanation for catalyst deactivation. The current findings do not support that catalyst deactivation is due to sintering of the active metal phase as reported before for Rh/SiO_2 during dry reforming of methane [79].

In an attempt to determine which effect is more important in explaining the stronger deactivation of the more dispersed Rh catalysts, the effect of the S/C ratio on the rate of catalyst deactivation was investigated. It is well known that a higher S/C ratio improves catalyst stability by reducing the formation of coke [80–83]. Fig. 15a shows the intrinsic reaction rate for Rh(0.1, 600)/ZrO_2(600) and Rh(1.6, 600)/ZrO_2(900) with initial dispersion of 83 and 24% after reduction, respectively, as a function of the time on stream for S/C ratios of 3 and 6. In line with our earlier finding, the catalytic activity does not depend on the S/C ratio. The rate of deactivation of Rh(0.1, 600)/ZrO_2(600) also does not depend on the S/C ratio. In order to verify whether the increased S/C ratio led to a decreased amount of carbonaceous deposits, TPO experiments were carried out after 15 h time on stream. Clearly, the amount of coke deposits has substantially decreased when the S/C ratio is 6 instead of 3 (Fig. 15b). For the small particle catalyst, the amount of coke is only half. These results clearly indicate that not carbon deposition but instead the oxidation of small nanoparticles is the dominant explanation for the deactivation of highly dispersed Rh catalysts.

5. Conclusions

The initial intrinsic surface atom reaction rate of steam methane reforming at 500 °C for a large set of Rh catalysts increases linearly with the metal dispersion. This points to dissociative methane adsorption as the rate-controlling step and is understood

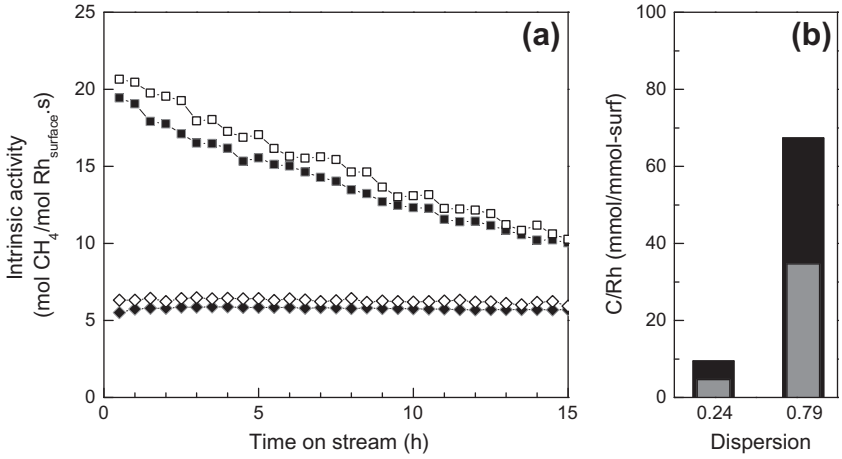

Fig. 15. (a) CH_4 steam reforming rates as a function of time on stream of (squares) Rh(0.1, 600)/ZrO_2(600) and (rhombi) Rh(1.6, 600)/ZrO_2(900) at S/C = 3 (closed) and S/C = 6 (open) (500 °C, 0.06 bar CH_4) and (b) the amount of carbon per surface metal atoms as a function of the S/C ratio (black: S/C = 3; gray: S/C = 6).

in terms of an increasing density of low-coordinated edge and corner metal atoms with decreasing particle size. C—O recombination is not the rate-controlling step, even when the temperature is lowered to 400 °C. The intrinsic activity does not depend on the type of support. The support only affects the catalytic activity in steam methane reforming indirectly by influencing the dispersion and the reduction degree of the metal phase.

Catalysts with Rh nanoparticles smaller than 2.5 nm deactivate more strongly than catalysts with larger nanoparticles. Characterization of spent catalysts by X-ray absorption spectroscopy shows that deactivation is due to the oxidation of very small particles under the steam methane reforming reaction conditions.

Acknowledgments

This research was performed within the framework of the EOS-LT program. The authors gratefully acknowledge Senternovem (Agentschap NL) of the Netherlands Ministry of Economic Affairs for financial support, NWO-Dubble for access to X-ray absorption spectroscopy facilities at ESRF, ESRF staff for their support and the Soft Matter Cryo-TEM Research Unit for access to the TEM facility. We thank Adelheid Elemans for the elemental analysis and Xian-Yang Quek for the TEM measurements.

References

[1] J.R. Rostrup-Nielsen, J. Sehested, J.K. Nørskov, Adv. Catal. 47 (102) (2002) 65–77.
[2] G.W. Huber, S. Iborra, A. Corma, Chem. Rev. 106 (2006) 4047–4059.
[3] J.R. Rostrup-Nielsen, Steam Reforming Catalysts, Danish Technical Press, Copenhagen, 1975. pp. 17–37.
[4] J. Sehested, Catal. Today 111 (2006) 104.
[5] J.R. Rostrup-Nielsen, J.H. Bak Hansen, J. Catal. 144 (1993) 40–41.
[6] D. Qin, J. Lapszewicz, Catal. Today 21 (1994) 552–555.
[7] G. Jones, J.G. Jakobsen, S.S. Shim, J. Kleis, M.P. Andersson, J. Rossmeisl, F. Abild-Pedersen, T. Bligaard, S. Helveg, B. Hinnemann, J.R. Rostrup-Nielsen, I. Chorkendorff, J. Sehested, J.K. Nørskov, J. Catal. 259 (2008) 147–160.
[8] A. Yamaguchi, E. Iglesia, J. Catal. 274 (2010) 52–63.
[9] M. Maestri, D.G. Vlachos, A. Beretta, G. Groppi, E. Tronconi, AlChE J. 55 (2009) 993–1008.
[10] J. Wei, E. Iglesia, J. Catal. 225 (2004) 116–127.
[11] J.K. Nørskov, T. Bligaard, J. Kleis, Science 324 (2009) 1655.
[12] R.A. van Santen, Acc. Chem. Res. 42 (2009) 57.
[13] R.A. van Santen, M. Neurock, S.G. Shetty, Chem. Rev. 110 (2009) 2027–2028.
[14] Z.P. Liu, P. Hu, J. Am. Chem. Soc. 125 (2003) 1961–1964.
[15] T. Zubkov, G.A. Morgan Jr., J.T. Yates Jr., O. Kühlert, M. Lisowski, R. Schillinger, D. Fick, H.J. Jänsch, Surf. Sci. 526 (2003) 57.
[16] J.K. Nørskov, T. Bligaard, A. Logadottir, S. Bahn, L.B. Hansen, M. Bollinger, H. Bengaard, B. Hammer, M. Mavrikakis, Y. Xu, S. Dahl, C.J.H. Jacobsen, J. Catal. 209 (2002) 276.
[17] R. van Hardeveld, F. Hartog, Surf. Sci. 15 (1969) 197.
[18] R. van Hardeveld, A. van Montfoort, Surf. Sci. 4 (1966) 416.
[19] S. Shetty, A.P.J. Jansen, R.A. van Santen, J. Am. Chem. Soc. 131 (2009) 12874–12875.
[20] S. Shetty, A.P.J. Jansen, R.A. van Santen, J. Phys. Chem. C 113 (2009) 19752.
[21] I.M. Ciobica, R.A. van Santen, J. Phys. Chem. B 107 (2003) 3811.
[22] O.R. Inderwildi, S.J. Jenkins, D.A. King, J. Am. Chem. Soc. 129 (2007) 1757.
[23] P.W. van Grootel, E.J.M. Hensen, R.A. van Santen, Langmuir 26 (2010) 16339–16348.
[24] M.P. Andersson, F. Abild-Pedersen, I.N. Remediakis, T. Bligaard, G. Jones, J. Engbæk, O. Lytken, S. Horch, J.H. Nielsen, J. Sehested, J.R. Rostrup-Nielsen, J.K. Nørskov, I. Chorkendorff, J. Catal. 255 (2008) 8–9.
[25] S. Shetty, R.A. van Santen, Phys. Chem. Chem. Phys. 12 (2010) 6330–6332.
[26] P.W. van Grootel, E.J.M. Hensen, R.A. van Santen, Surf. Sci. 603 (2009) 3277–3280.
[27] M.J.T.C. van der Niet, A. den Dunnen, L.B.F. Juurlink, M.T.M. Koper, Angew. Chem. Int. Ed. 49 (2010) 6572–6575.
[28] Y. Li, Q. Fu, M. Flytzani-Stephanopoulos, Appl. Catal. B 27 (2000) 181.
[29] Y. Guan, E.J.M. Hensen, Phys. Chem. Chem. Phys. 11 (2009) 9578.
[30] H.X. Mai, L.D. Sun, Y.W. Zhang, R. Si, W. Feng, H.P. Zhang, H.C. Liu, C.H. Yan, J. Phys. Chem. B 109 (2005) 24381–24384.
[31] J.J.F. Scholten, Catal. Rev. Sci. Eng. 27 (1985) 151–206.
[32] R.H. Schroder, N. Schmitz-Pranghe, R. Kohlhaas, Zeitschrift fur metallkunde 62 (1972) 12.
[33] J.M.D. Coey, Acta Crystallogr. Sect. B 26 (1970) 1876.
[34] Y. Zhou, J.M. Perket, J. Zhou, J. Phys. Chem. C 114 (2010) 11853–11860.
[35] . Martin, D. Duprez, Appl. Catal. A 131 (1995) 298.
[36] A. Karpenko, R. Leppelt, V. Plzak, J. Cai, A. Chuvilin, B. Schumacher, U. Kaiser, R.J. Behm, Top. Catal. 44 (2007) 183–187.
[37] R. Si, M. Flytzani-Stephanopoulos, Angew. Chem. Int. Ed. 47 (2008) 2886.
[38] K. Zhou, X. Wang, X. Sun, Q. Peng, Y. Li, J. Catal. 229 (2005) 209.
[39] M. Mogensen, in: Trovarelli (Ed), Catalysis by Ceria and Related Materials, Catalytic Science Series, ICP, vol. 15, 2002, p. 465 (Chapter 4).
[40] X. Liu, K. Zhou, L. Wang, B. Wang, Y. Li, J. Am. Chem. Soc. 131 (2009) S5.
[41] S. Eriksson, S. Rojas, M. Boutonnet, J.L.G. Fierro, Appl. Catal. A 326 (2007) 12.
[42] G. Colón, M. Pijolat, F. Valdivieso, H. Vidal, J. Kašpar, E. Finocchio, M. Daturi, C. Binet, J.C. Lavalley, R.T. Baker, S. Bernal, J. Chem. Soc. Faraday Trans. 94 (1998) 3720.
[43] C.E. Hori, H. Permana, K.Y.S. Ng, A. Brenner, K. More, K.M. Rahmoeller, D. Belton, Appl. Catal. B 16 (1998) 107–109.
[44] V. Perrichon, L. Retailleau, P. Bazin, M. Daturi, J.C. Lavalley, Appl. Catal. A 260 (2004) 4–5.
[45] J.M. Gatica, R.T. Baker, P. Fornasiero, S. Bernal, G. Blanco, J. Kašpar, J. Phys. Chem. B 104 (2000) 4667.
[46] D.C. Koningsberger, J.B.A.D. van Zon, H.F.J. van't Blik, G.J. Visser, R. Prins, A.N. Mansour, D.E. Sayers, D.R. Short, J.R. Katzer, J. Phys. Chem. 89 (1985) 4075–4081.
[47] J. Cunningham, D. Cullinane, J. Sanz, J.M. Rojo, X.A. Soria, J.L.G. Fierro, J. Chem. Soc. Faraday Trans. 88 (1992) 3236.
[48] S. Bernal, J.J. Calvino, M.A. Cauqui, J.M. Gatica, C. López Cartes, J.A. Pérez Omil, J.M. Pintado, Catal. Today 77 (2003) 393–403.
[49] W. Liu, A.F. Sarofilm, M. Flytzani-Stephanopoulos, Chem. Eng. Sci. 49 (1994) 4871.
[50] J.T. Miller, A.J. Kropf, Y. Zha, J.R. Regalbuto, L. Delannoy, C. Louis, E. Bus, J.A. van Bokhoven, J. Catal. 240 (2006) 222–234.
[51] J.B.A.D. van Zon, D.C. Koningsberger, H.F.J. van't Blik, D.E. Sayers, J. Chem. Phys. 82 (1985) 5752.
[52] A.J. Dent, J. Evans, S.G. Fiddy, B. Jyoti, M.A. Newton, M. Tromp, Faraday Discuss. 138 (2008) 292.
[53] J.D. Grunwaldt, L. Basini, B.S. Clausen, J. Catal. 200 (2001) 324.
[54] A. Gayen, K.R. Priolkar, P.R. Sarode, V. Jayaram, M.S. Hedge, G.N. Subbanna, S. Emura, Chem. Mater. 16 (2004) 2322–2326.
[55] G. Vlaic, P. Fornasiero, G. Martra, E. Fonda, J. Kašpar, L. Marchese, E. Tomat, S. Coluccia, M. Graziani, J. Catal. 190 (2000) 184.
[56] A. Siani, O.S. Alexeev, D.S. Deutsch, J.R. Monnier, P.T. Fanson, H. Hirata, S. Matsumoto, C.T. Williams, M.D. Amiridis, J. Catal. 266 (2009) 335–338.
[57] H. Kusama, K.K. Bando, K. Okabe, H. Arakawa, Appl. Catal. A 197 (2000) 259.
[58] H. Tanaka, R. Kaino, K. Okumura, T. Kizuka, Y. Nakagawa, K. Tomishige, Appl. Catal. A 378 (2010) 178–181.
[59] M. Lepage, T. Visser, F. Soulimani, A.M. Beale, A. Iglesias-Juez, A.M.J. van der Eerden, B.M. Weckhuysen, J. Phys. Chem. C 112 (2008) 9396.
[60] T.G. Ros, D.E. Keller, A.J. van Dillen, J.W. Geus, D.C. Koningsberger, J. Catal. 211 (2002) 94.
[61] J.F. Goellner, B.C. Gates, J. Phys. Chem. B 105 (2001) 3276.
[62] W.A. Weber, B.C. Gates, J. Phys. Chem. B 101 (1997) 10433.
[63] B.J. Kip, F.B.M. Duivenvoorden, D.C. Koningsberger, R. Prins, J. Catal. 105 (1987) 26–38.
[64] J.G. Jakobsen, T.L. Jørgensen, I. Chorkendorff, J. Sehested, Appl. Catal. A 377 (2010) 161.
[65] A.M. Baele, B.M. Weckhuysen, Phys. Chem. Chem. Phys. 12 (2010) 5562–5574.
[66] B.S. Bunnik, G.J. Kramer, J. Catal. 242 (2006) 314.
[67] R.A. van Santen, M. Neurock, Molecular Heterogeneous Catalysis, first ed., Wiley-VCH, Weinheim, 2006. pp. 27–126 (Chapters 2–3).
[68] M. Zeppieri, P.L. Villa, N. Verdone, M. Scarsella, P. De Filippis, Appl. Catal. A 387 (2010) 153–154.
[69] M. Mavrikakis, M. Bäumer, H.J. Freund, J.K. Nørskov, Catal. Lett. 81 (2002) 154.
[70] A.P. Ferreira, D. Zanchet, J.C.S. Araújo, J.W.C. Liberatori, E.F. Souza-Aguiar, F.B. Noronha, J.M.C. Bueno, J. Catal. 263 (2009) 335–344.
[71] L.S.F. Feio, C.E. Hori, S. Damyanova, F.B. Noronha, W.H. Cassinello, C.M.P. Marques, J.M.C. Bueno, Appl. Catal. A 316 (2007) 107–116.
[72] R. Craciun, W. Daniell, H. Knözinger, Appl. Catal. A 230 (2002) 153–168.
[73] R. Craciun, B. Shereck, R.J. Gorte, Catal. Lett. 51 (1998) 149–153.
[74] S. Ricote, G. Jacobs, M. Milling, Y. Ji, P.M. Patterson, B.H. Davis, Appl. Catal. A 303 (2006) 35.
[75] R.J. Gorte, AlChE J. 56 (2010) 1126.
[76] A. Erdöhelyi, J. Cserényi, F. Solymosi, J. Catal. 141 (1993) 287–299.
[77] M.E. Grass, Y. Zhang, D.R. Butcher, J.Y. Park, Y. Li, H. Bluhm, K.M. Bratlie, T. Zhang, G.A. Somorjai, Angew. Chem. Int. Ed. 47 (2008) 8893–8896.
[78] D.A.J.M. Ligthart, R.A. van Santen, E.J.M. Hensen, Angew. Chem. Int. Ed., in press, doi:10.1002/anie.201100190.
[79] J.H. Bitter, K. Seshan, J.A. Lercher, J. Catal. 176 (1998) 95.
[80] F. Moseley, R.W. Stephens, K.D. Stewart, J. Wood, J. Catal. 24 (1972) 26–27.
[81] C.H. Bartholomew, Catal. Rev.-Sci. Eng. 24 (1982) 88.
[82] M. Belgued, P. Pareja, A. Amariglio, Nature 352 (1991) 789.
[83] R.M. Rioux, A.L. Mash, J.S. Gaughan, G.A. Somorjai, Catal. Today 123 (2007) 274–275.